5-12-2024

Robust Fault Location in Power Systems Transmission Lines Based on Traveling Waves Using Multiple Wavelet Types in an Ensemble Model

Mirjavad Hashemi Gavgani
Syracuse University

ABSTRACT

Abstract_ Fault location plays a vital role in the operation of power systems. It is the key to fast clearance of the faults and minimizing the duration and costs of power outages. Power networks manifest a complex behavior due to their intricate topological connections, phase asymmetry, and time-varying loads. Traveling Wave (TW) analysis provides an accurate estimate of fault location on the power system transmission lines. In this project, we explore the main concepts and steps of implementing traveling waves for fault location and different methodologies for extracting and analyzing the traveling waves using different wavelets. Then, we present an ensemble approach for robust detection of the Time of Arrival for traveling waves using a large group of wavelet types. The implemented approach is tested on real-world measurement data from a transmission-level substation. The robustness of the method is tested in different noise scenarios. The results show significantly accurate and robust performance of the developed scheme for determining fault location.

ROBUST FAULT LOCATION IN POWER SYSTEMS TRANSMISSION LINES BASED ON TRAVELING WAVES USING MULTIPLE WAVELET TYPES IN AN ENSEMBLE MODEL

by

Mirjavad Hashemi Gavgani

B.S., Iran University of Science and Technology, 2013
M.S., Shahid Beheshti University, 2016

Dissertation
Submitted in partial fulfillment of the requirements for the degree of
Doctor of Philosophy in Electrical and Computer Engineering.

Syracuse University
May 2024

ACKNOWLEDGEMENTS

I want to extend my heartfelt gratitude to those individuals and entities whose invaluable support and contributions were essential to the successful completion of this research.

Firstly, I want to thank my advisors, Dr. Can Isik and Dr. Tomislav Bujanovic, for their unwavering support, guidance, and mentorship throughout this project.

I am thankful to the committee members – Dr. Edward Bogucz, Dr. Makan Fardad, Dr. Younes Ra'di, and Dr. Ilya Grinberg – for their valuable insights and constructive feedback, which significantly enriched the research.

The institutional backing from Syracuse University and National Grid played a critical role in completing this research. I am grateful to both these entities for providing essential resources, facilities, and sample data.

I thank my dear wife, Matin, whose presence, support, and steadfast belief in me is the reason why this document exists.

I express profound appreciation to my parents for their sacrifices and encouragement, which have been the bedrock upon which I built my dreams.

A special acknowledgment is extended to my valued research partner, friend, and life coach, Larry Durante, whose dedication to our shared goals has made a lasting impact on every page of this document.

Lastly, I want to dedicate this document to the vibrant community of Syracuse University graduate students for their camaraderie and shared journey.

TABLE OF CONTENTS

LIST OF TABLES

LIST OF FIGURES

CHAPTER 1

INTRODUCTION

1.1 Fault Location in Power Systems

As the penetration of renewable energy resources increases in power systems, the dynamics of power systems are changing dramatically. These changes are mainly induced by the inverter-based connection of the renewable energy resources, which do not have the luxury of solid frequency support in contrast to the rotating generators. As a result of these changes, safeguarding the security of power systems and maintaining their stability has become a challenging task that engenders the evolution of protection schemes and enhancements in situational awareness tools [1].

Protection schemes are required to meet two main criteria: 1. Sensitivity 2. Selectivity. Sensitivity is the quality of detection and isolation of the faults promptly so that the faults do not cascade or harm the other equipment in the system. Selectivity is the capability of identifying the optimum schemes for isolating the fault to minimize the outage duration and the number of customers affected. [2].

Protection Fault Location (FL) is a critical component of power system protection schemes since it is the core task for implementing circuit breakers and restoration. In general, the schemes for fault location are categorized into two groups [3]:

1. Power-frequency level signal analysis (Impedance-Based Method)
2. High-frequency signal analysis (Traveling-Wave-Based Method).

Impedance-based methods are based on three approaches

1. single-end

2. double-end

3. multi-end

Single-end approaches detect the location of the fault based on the measurements from only one side of the transmission line [4–6]. The authors in [7] have proposed a single-end fault location method that operates on the reactance of the faulty line calculated based on the voltage and current measured at one end of the line. Following the same method, authors in [8] use a compensation technique to enhance the accuracy of the impedance-based method considering the effects of remote-end in-feed of the transmission line by analyzing the complete model of the interconnections in the network. Moreover, the authors in [9] use a single-end impedance-based fault location method for double-circuit transmission lines. The proposed method in this paper is based on modifying the apparent impedance by utilizing modal transformation. To address some inaccuracies in the aforementioned methods, the authors in [10] propose a method based on the pre-fault voltage and current measurements combined with post-fault voltage measurements. The post-fault current measurements were omitted to minimize the effect of transformer saturation current.

Double-ended approaches use the measurements from both ends of a transmission line to determine the location of the fault on the line [11–14]. In one of the early attempts at this approach, the authors of [15] propose a fault analysis method based on synchronized measurements from both ends of the transmission line. Their approach is based on the lumped parameter transmission line modeling and implementation of measurements from both ends to classify and locate the fault on the transmission line. On the other hand, authors in [16] implement an iterative method using unsynchronized phasor measurements from both ends of the transmission line distributed model to locate the fault. This search method executes iterative linear approximations of voltage and current at both ends of the transmission line, leading to a common point that represents the

fault location. This algorithm liberates the operator from the need for synchronized measurements and produces a reasonably accurate estimate of the fault location. Similarly, authors in [17] have used unsynchronized voltage and current measurements from both ends of the line for fault location. By combining the pre-fault and post-fault data, the authors have developed an algorithm that estimates the distributed line parameters and makes it robust to line shunt capacitance values.

1.2 Traveling Waves

Traveling-wave-based methods have emerged as promising tools for fast and accurate fault location in power system transmission lines [18]. These methods are basically indebted to the theoretical electromagnetic wave propagation theory foundations laid by pioneering physicists like Oliver Heaviside and Charles Legeyt Fortescue [19]. These core concepts have gained wide use for fault detection and location upon advancements in synchro-phasor measurements and high-frequency sensors deployed in power systems [20].

Fundamentals of fault location based on Traveling Waves encompasses the investigation of high-frequency measured signals for detecting the time of arrival (TOA) for the signature wave of the fault [21]. The high-frequency electromagnetic transients (waves) created by fault travel in both directions on the transmission line as displayed in figure 1.1 with a velocity close to the speed of light [22]. This diagram is referred to as the lattice diagram or Bewley's diagram and plays an important role in visualizing the propagation behavior of fault-generated waves on the transmission line.

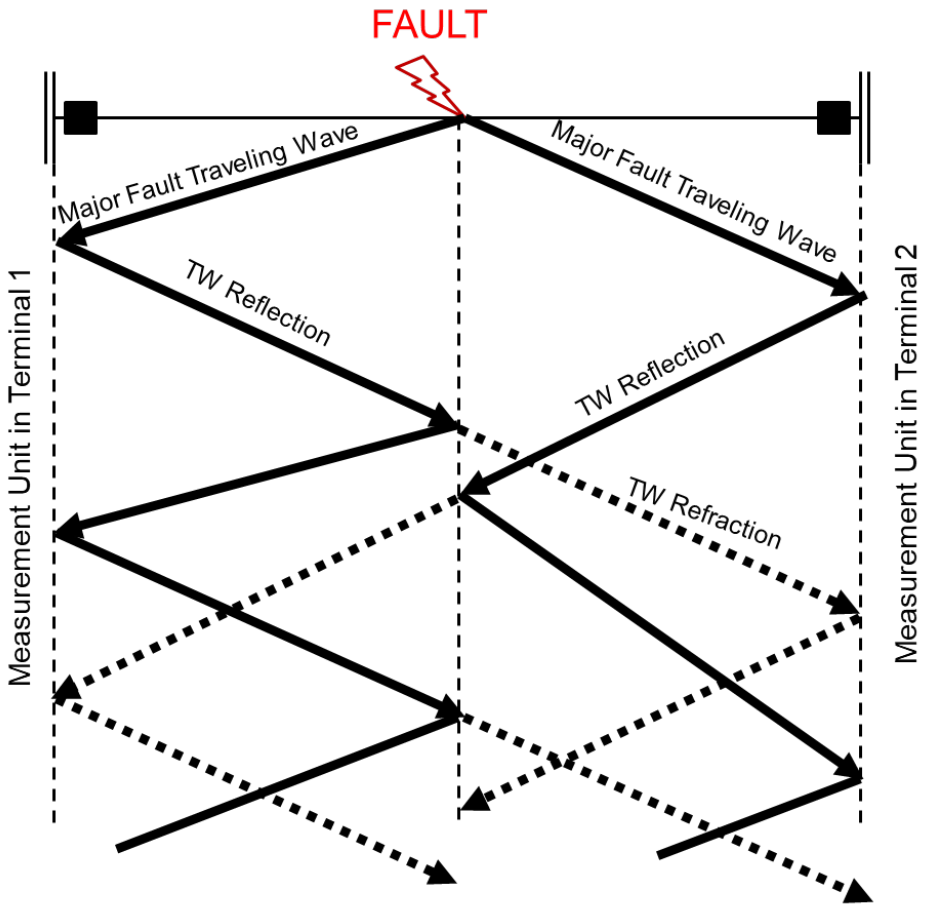

Figure 1.1: Example of Bewley's Diagram, representing the traveling directions of the fault-generated waves

1.2.1 Telegrapher's Equations

The voltage and current of the waves described in figure 1.1 are mainly regulated by *Telegrapher's* equations. These equations are in the form of coupled voltage and current differential equations with space and time as variables as follows [23]:

$$\frac{\partial}{\partial x}V(x,t) = -L\frac{\partial}{\partial t}I(x,t) - RI(x,t) \tag{1.1}$$

$$\frac{\partial}{\partial x}I(x,t) = -C\frac{\partial}{\partial t}V(x,t) - GV(x,t) \tag{1.2}$$

Where R, L, G, and C are the transmission line's per-unit resistance, inductance, conductance, and capacitance.

Telegrapher's equations can be simplified in the phasor domain of power systems as follows [24]:

$$\tilde{I}(x,t) = I_0^+ e^{-\gamma x} + I_0^- e^{+\gamma x} \tag{1.3}$$

$$\tilde{V}(x,t) = V_0^+ e^{-\gamma x} + V_0^- e^{+\gamma x} \tag{1.4}$$

where $I_0^+, I_0^-, V_0^+, V_0^-$ represent the Laplace transforms of the forward and backward traveling (+ for forward, and − for backward traveling) current and voltage waves for sinusoids with different frequencies. Propagation constant γ is a line characteristic that is comprised of attenuation constant α and phase constant β as described below:

$$\gamma = \alpha + j\beta \tag{1.5}$$

By plugging in the values from 1.1 and 1.2 in the resulting phasor equations it is derived that:

$$\gamma = \sqrt{(R + j\omega L)(G + j\omega C)} \tag{1.6}$$

It is important to note that the transmission line acts as the medium for propagation of the wave traveling on it. The β parameter of the transmission line plays a key role in determining the velocity of propagation for different frequency components of the traveling wave. This relationship is governed by the following equation [25]:

$$v = \frac{\omega}{\beta} \tag{1.7}$$

As the angular frequency of the traveling wave increases, this velocity approaches the speed of light c.

1.2.2 Traveling Wave Component Extraction

System Frequency Level Components

The equations presented in section 1.2.1 obviate that extracting the main frequency components of a Traveling Wave from the measured signal is the key step for properly employing it for fault location. Many signal-processing approaches have been implemented by researchers to meet this goal. In this section, we delve into some of these approaches.

The measured signal is prone to containing some system frequency level components at 60 Hz and its multiples, (mostly in the Americas, and 50 Hz and its integer multiples in the rest of the world) which need to be filtered out using a high-pass filter. These steady state components are injected from power system equipment during the fault and might distort the measured signal and falsify the peak point calculation that is relied on for determining the TOA of the traveling wave. an example of such frequency level components is visible in a study case shown in figure 1.2. The time domain signal has some visibly strong low-frequency components driving it. A close look at the frequency spectrum of this measured signal 1.3 validates the concern for presence of system-level frequencies in the measured signal.

After conditioning the measured signal with a high-pass filter, proper signal processing methods should be applied to extract the shape of the high-frequency traveling wave from this signal. In most approaches, the goal is to detect the time point of the peak or wavefront of the traveling wave as the representative of the distance that wave has traveled. For example, in [26], this peak is calculated by extrapolating the resultant parabola from smoothing and differentiating the conditioned signal.

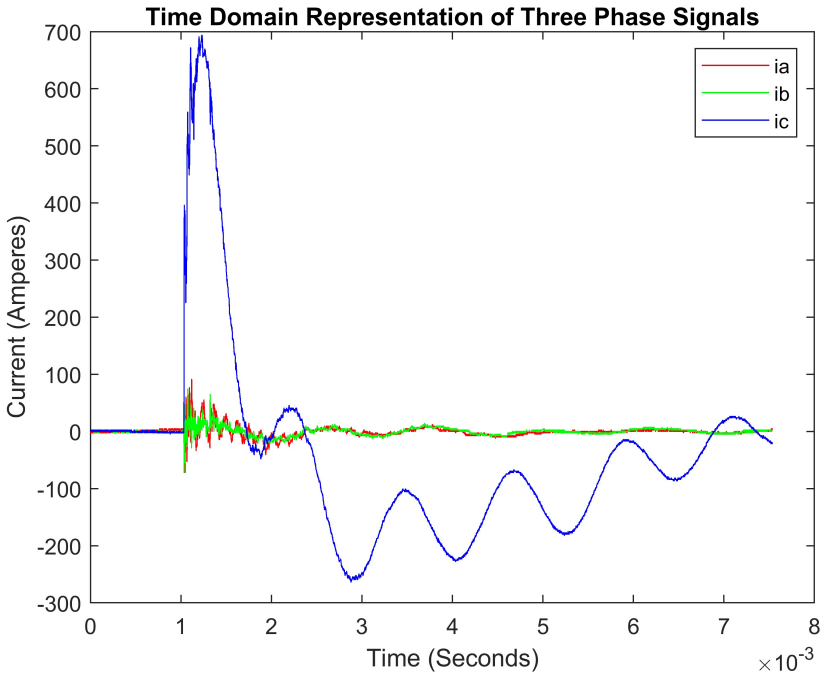

Figure 1.2: Example of presence of system frequency level components in the measured signal

Wavelet Transform

When it comes to advanced signal processing, time and frequency accuracy dilemma appears to be one of the main challenges that scientists and engineers need to address properly based on the nature of their research. The root cause that makes this problem challenging is the time-frequency uncertainty principle which is very similar to the position-momentum uncertainty principle. Based on the time-frequency uncertainty principle [27], the more accurately you know about the time domain characteristics of a signal, the less accurately you can know about the frequency domain values of that signal. In other words:

$$\Delta t \cdot \Delta f \geq \frac{1}{4\pi} \tag{1.8}$$

where Δt is the uncertainty in time and Δf is the uncertainty in frequency components or spread. Therefore, as we make the analysis window smaller for a more accurate time

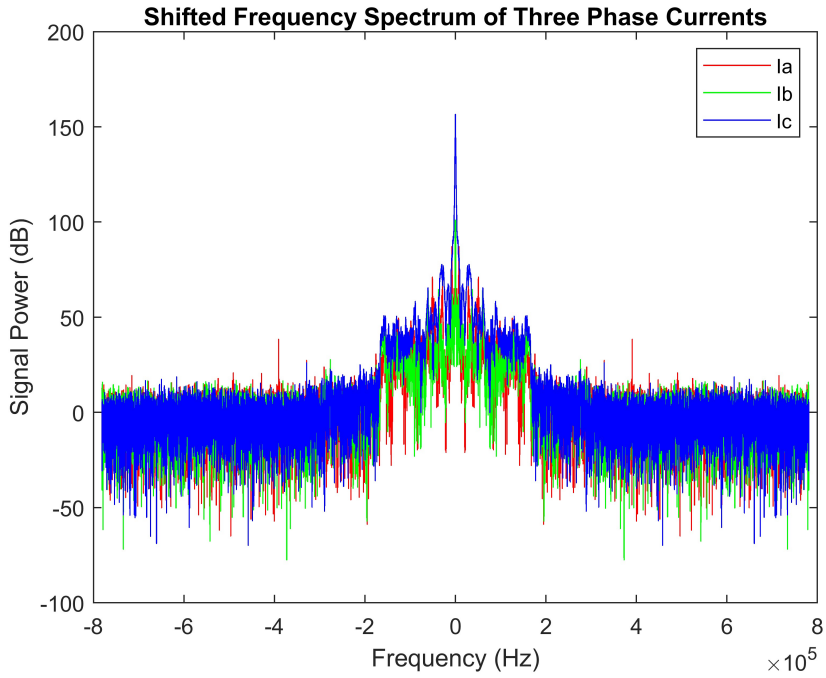

Figure 1.3: Double side band frequency domain representation of the measured signal with high system frequency level components

domain analysis, our frequency resolution drops, and as we make the analysis window larger for higher resolution frequency analysis, we lose sight of time domain details. For example, when we conduct Fourier analysis on a large time window for a higher frequency resolution, we are never sure when the resulting frequencies have happened.

Wavelet Transform is an effective and widely used mathematical signal processing tool that somewhat bridges the time-frequency dilemma gap. The localization capability of wavelets in time and frequency enables researchers and engineers to capture the rapid signal changes, which may be viewed from time-domain, frequency-domain or a combined perspective. Continuous wavelet transform(CWT) is formulated as follows [28]:

$$CWT(a,b) = \int_{-\infty}^{\infty} x(t) \cdot \frac{1}{\sqrt{a}} \cdot \psi^* \left(\frac{t-b}{a} \right) dt \tag{1.9}$$

where $x(t)$ is our time domain studied signal, $\psi(t)$ is the mother wavelet, a is the scaling parameter, and b is the shifting parameter that moves the scaled mother wavelet across

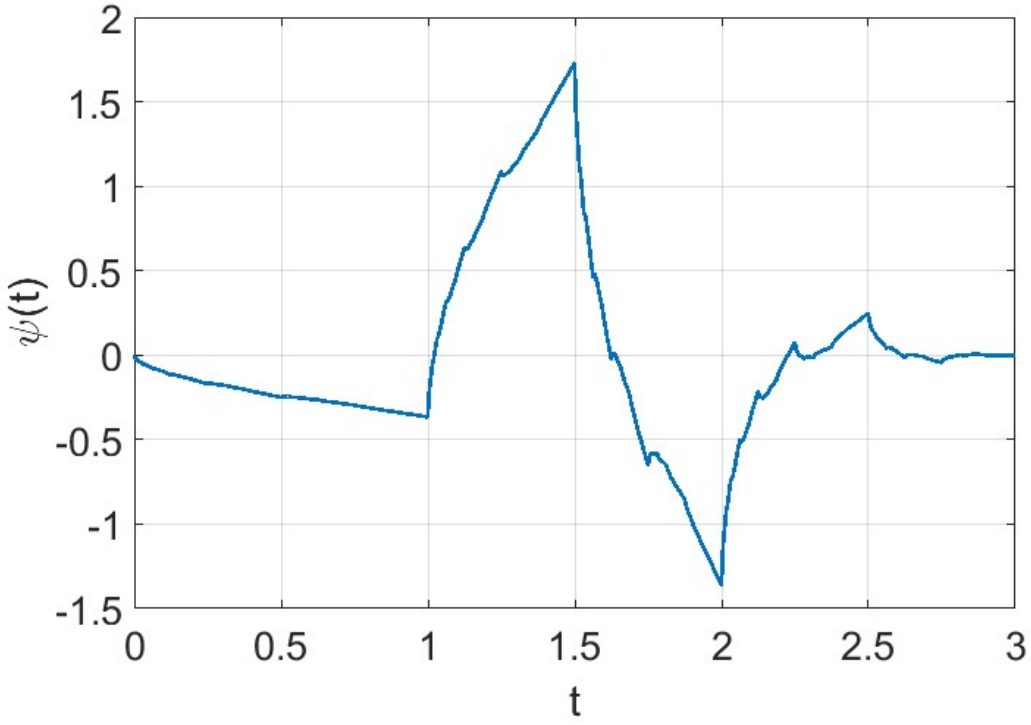

Figure 1.4: Daubechies 2 (db2) Mother Wavelet

the studied signal. Figure 1.4 shows the mother wavelet for Daubechies 2 wavelet.

Continuous wavelet transform is usually of theoretical interest, since most signals are collected using digital methods. Therefore, Discrete-time wavelet transform (DWT) is utilized in almost all practical applications. DWT works based on filtering operations and down-sampling the signal. For DWT, we need to form filter banks. For example, let's consider $x[n]$ to be the input signal, $h[n]$ to be the high pass filter and $g[n]$ the low pass filter. These two filters are utilized to decompose the main signal $x[n]$ into two Approximation and Detail signals:

$$A[j,k] = \left(x * h_{j,k}\right)[2k] \tag{1.10}$$

$$D[j,k] = \left(x * g_{j,k}\right)[2k] \tag{1.11}$$

where $h_{j,k}[n] = 2^{j/2}h[2^n - k]$ is the scaled and translated high pass filter and $g_{j,k}[n] = 2^{j/2}g[2^n - k]$ is the scaled and translated low-pass filter. The signal is down-sampled as it

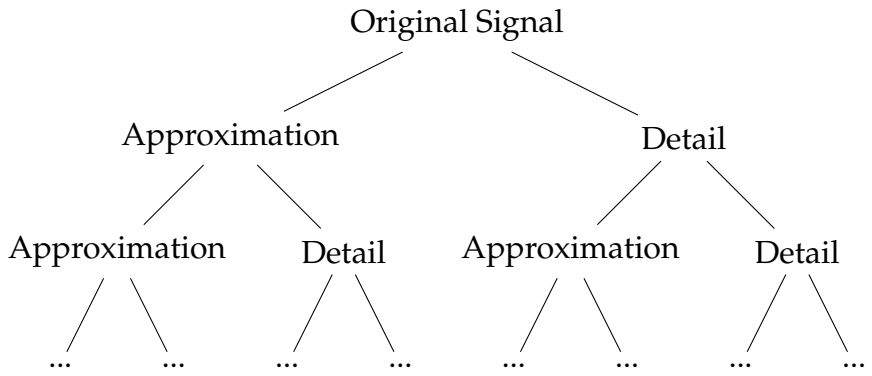

Figure 1.5: Wavelet Tree Diagram

gets filtered by the low-pass and high-pass filters of the filter bank.

This process can continue on multiple levels to extract more detailed information from the signal stored in the format of a Wavelet Tree, as shown in figure 1.5 [29] [30]. This tree can be further reduced in size by only keeping the essential information needed for the reconstruction of the signal, as shown in figure 1.6. This reduced tree is called a Multi-resolution analysis (MRA) tree. MRA tree practically leaves out the redundant nodes of the Wavelet tree and keeps only enough information to reconstruct the signal from bottom to top. Moving down in the MRA tree, the signal passes through low-pass filters of the employed wavelet when branched to the left, and the resulting signal is called an Approximation signal. An example low pass filter for the Daubechies2 wavelet is shown in figure 1.7 [31]. When we branch to the right, the signal passes through a high-pass filter, and the resulting signal is called a Detail signal. Figure 1.8 shows an example of db2 high-pass filter coefficients.

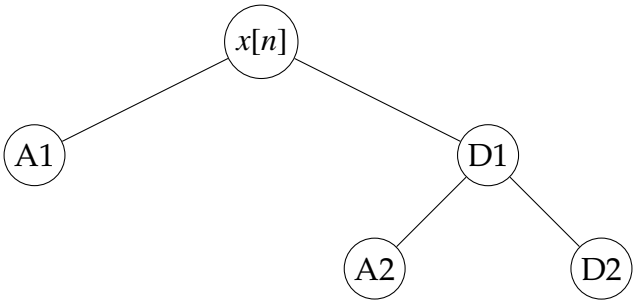

Figure 1.6: MRA Wavelet Tree Diagram

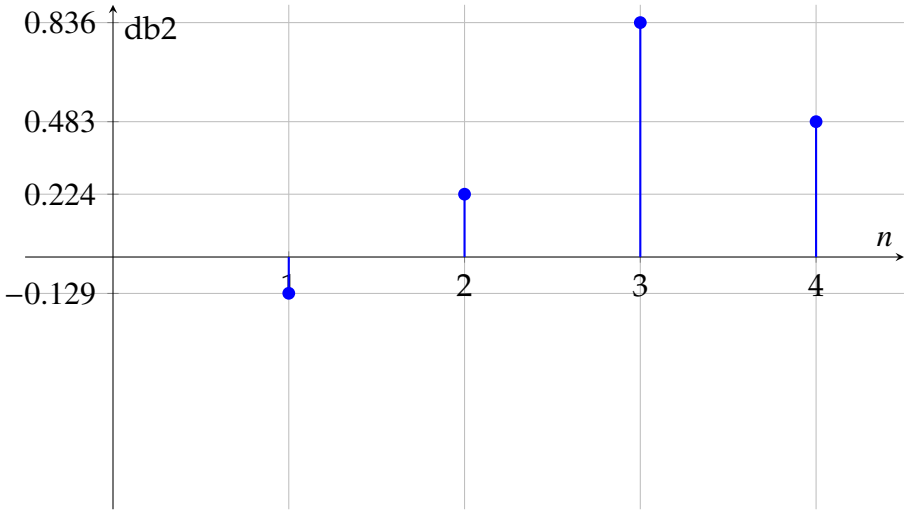

Figure 1.7: Decomposition Low-Pass Filter Coefficients for db2 wavelet

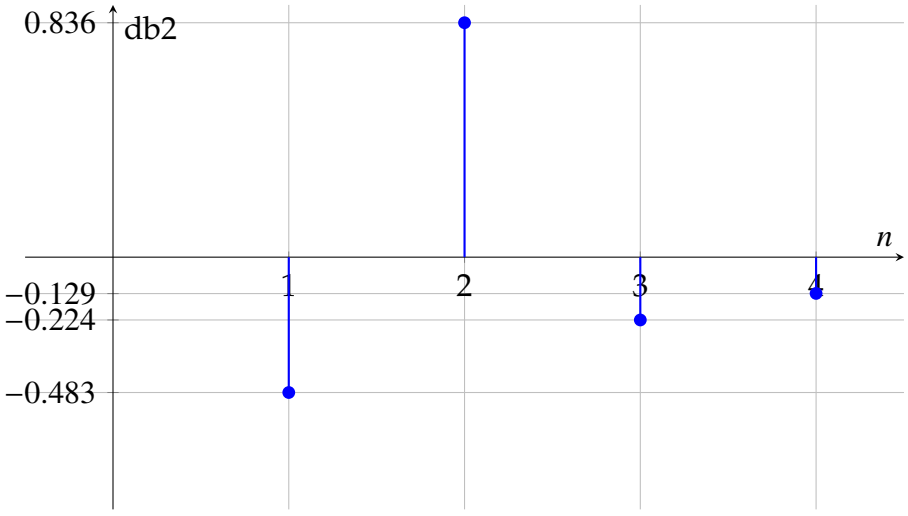

Figure 1.8: Decomposition High-Pass Filter Coefficients for db2 wavelet

1.3 Approaches and Shortcomings in Current Literature

Traveling Wave-based fault location in power systems has been extensively explored in the past few decades. A majority of contemporary research about TW-based fault location on transmission lines is based on simulation-based data [20,22,32–34]. These simulations are mainly carried out using ATP [6,35–37], EMTP-RV [4,38], PSCAD-EMTDC [20], and RTDS [14] platforms.

As thoroughly discussed in [39], the real-world traveling waves created by short-circuit faults significantly differ from those observed in simulations-based research projects. While acknowledging the merit of the state-of-the-art signal processing approaches presented in these research works, it should be noted that their implementation on real-world data is questionable in terms of reliability, performance, and robustness [39,40].

The wavelet types used for detection in different scenarios are a point of debate. The majority of research works have utilized Daubechies 1, 4, or 8, with the claim that they are superior in performance since they are compactly supported with extremal phase, have a high number of vanishing moments, and are equipped with minimum-phase filters as scaling filters [30,33,41]. The limitations and accuracy of using these wavelets in real-world data are questioned in [39], which has adopted the Biorthogonal 2.2 wavelet for fault location on real-world data instead. It is later discussed by the first two authors of that work [40] that real-world TWs manifest unpredictable non-stationary random waveforms that might not be capturable by a single wavelet shape, resorting to statistical approaches. Some research works have developed their own customized wavelets for fault location using modified wavelet transform (MODWT) [32] or Empirical Wavelet Transform (EWT) [34]. The search for creating an optimal wavelet type has been mainly focused on enhancing the ”peakedness” of the detected traveling wave, however based

on the discussion in [40] and also the transient behavior of CTs and PTs considered, there is no one-cure-for-all in suitable wavelet shape for detecting TWs.

In another view, there is a noticeable absence of robustness discussions and performance analysis under adverse conditions such as strong noise or attack. A few research works have presented specific scenarios with added Gaussian noise to their studied signals to verify the robustness of their methods. However, there is a lack of discussion on the uncertainty added by down-samplings of the wavelet tree or the SNR of the noisy signal examined. For example, in [33], a very high accuracy in the range of meters is calculated for a specific simulation-base scenario, which can work by chance. However, the fact that the uncertainty for the detected location in the frequency of 1 MHz using the 4th level of the db8 wavelet tree is prone to be up to 1.75 Miles is overlooked. The robustness studies in [22] are also implemented on a signal without specifications on the SNR, which can be easily calculated to be about 20dB for the tested scenario. But this noise level still keeps the signal at an acceptable quality, far from adverse conditions.

The contribution of this research is to use an assembly of wavelets from different families with different characteristics of orthogonality, smoothness, localization, vanishing moments, symmetry, number of coefficients, and filter length in a strategically harmonized approach to detect the presence and arrival time of the traveling wave in a measured signal. This approach accounts for the randomness and unpredictability of wave shapes for fault-induced traveling waves discussed in [40]. We have adopted a single-ended approach for this analysis to remove the dependency of the method's reliability on communication links of the measurement units at two ends of the transmission line. It should be noted that the method introduced here can be easily adapted for double-ended and multi-ended schemes. This possibility is noted in the future research section. The implemented method is founded on a novel design of an automatic fault inception detection algorithm that alleviates subjectivity and human interaction issues pinpointed in [39].

The results are provided with confidence intervals and uncertainty in the estimated fault location. The method's robustness is tested under adverse conditions of noise attacks. The performance of the scheme is tested on real-world anonymized measurements provided by National Grid.

The rest of this dissertation is structured as follows: in Chapter 2, the different steps of this methodology are explained; in Chapter 3, implementation results are presented and explained; in Chapter 4, the conclusions and future work are discussed.

CHAPTER 2

METHODOLOGY

2.1 Introduction

In this research, we have designed a scheme for multiple wavelet types to contribute to detecting a traveling wave and estimating its time of arrival in a measured signal for fault location purposes.

The major contributions of this research are:

1. Design and Development of a scheme for Fault Location (FL) on transmission lines based on detecting Time of Arrival (TOA) for Traveling Waves (TW)using a combination of Wavelet Transforms (WT).
2. Provide a visual tool for understanding different detection results by different wavelets as a platform to help understand the fault situation and also tune the problem parameters.
3. Provide a comprehensive analysis of the performance of different wavelet types based on the statistical and engineering analysis of final results.

The outline of our approach to meet the goals above includes the following major steps:

1. Conditioning the measured signal, which entails filtering out the system frequency level components and digitization noise from the measured signal.
2. Multi-Resolution Analysis (MRA) using wavelet tree for candidate wavelet types.

3. Segmentation of the each node from MRA analysis to identify Measurement occurrences (MOs).
4. Creating a database of detected MOs with essential characteristics stored for each MO.
5. Ensemble voting and refining the MO database
6. Decision-Making on the conclusiveness of results for each node
7. Formation of database for fault location predictions made by each wavelet type
8. Validation of calculated fault locations based on time/frequency correlation of the first and second packets detected by each wavelet type in the studied range of frequency
9. Ensemble voting process on the calculated fault locations
10. Providing highest vote results as the fault location results along with the uncertainty range and confidence interval based on the wavelet tree level it is calculated in.
11. Robustness test under heavy noise

Figure 2.1 shows a block diagram of steps for the implemented scheme.

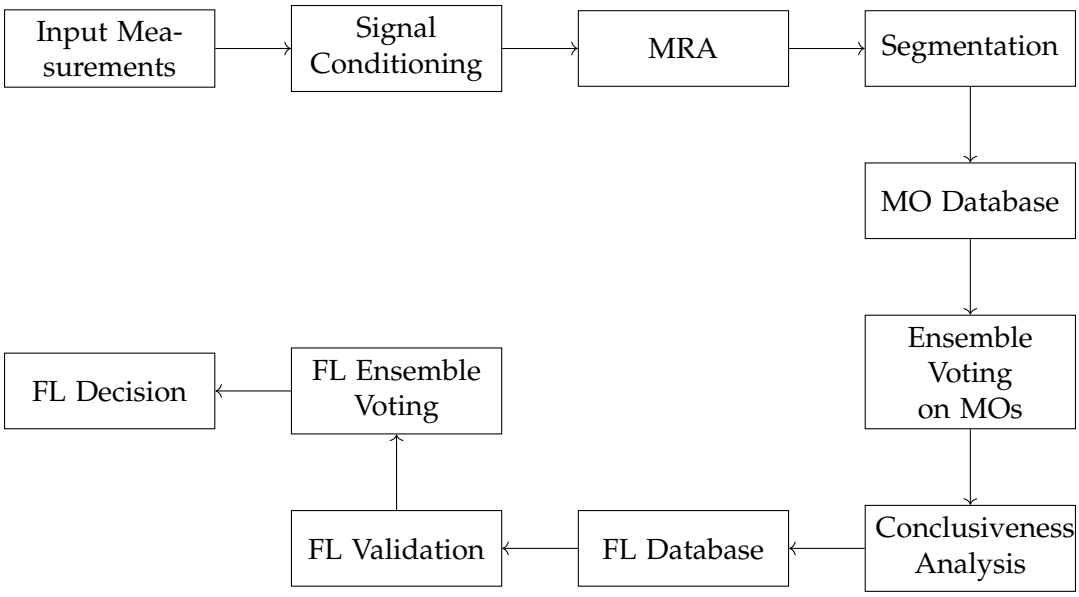

Figure 2.1: Block diagram of the steps for the implemented scheme

2.2 Conditioning the Measured Signal

As discussed in Section 1.2.2, the first step for TW analysis is to condition the measured signal by filtering out the frequency components that originate from power system components or measurement unit digitization. An example of system-level frequency components in a TW measured signal was presented in figure 1.2. As it is observed in figure 1.3 60 Hz component and its respective harmonics appear in the lower end of the frequency spectrum for the measured signal, and we can filter them out using a high-pass filter. On the other hand, there are some high-frequency components that are introduced as a result of digitization in Relay measurements. Figure 2.4 shows an example of such noises. This figure is an enlarged view of the same set of signals present in figure 1.2. These noises are very close to the Nyquist frequency of the measurement system and can be filtered out by using a low-pass filter. The frequency response of a generic high-pass filter is shown in figure 2.2.

A Band-Pass filter can be employed to remove the frequency components from the two

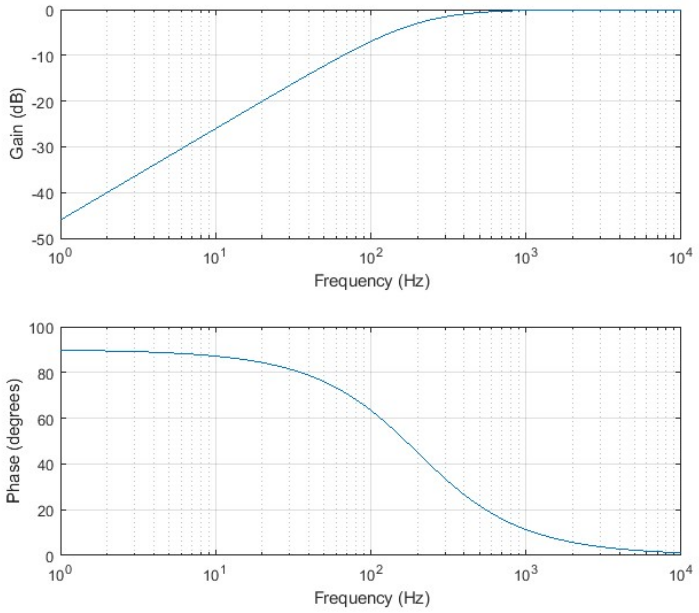

Figure 2.2: Generic Frequency Response of First-Order RC High-Pass Filter

ends of signal pertaining to the system frequency level and digitization noise. Here we have implemented an ideal band-pass filtering with a square window that only handpicks the frequency components within the studied range. This scheme works because our sampling frequency is so much higher than the studied range and approaching frequency filtering with a rectangle shape filter does not introduce impurities to signal behavior. Figure 2.6 shows how this ideal filter leaves out the system frequency level components compared to *ic* signal in figure 2.4. Figure 2.5 shows how the digitization noise is removed from the signal compared to *ic* signal in figure 1.2.

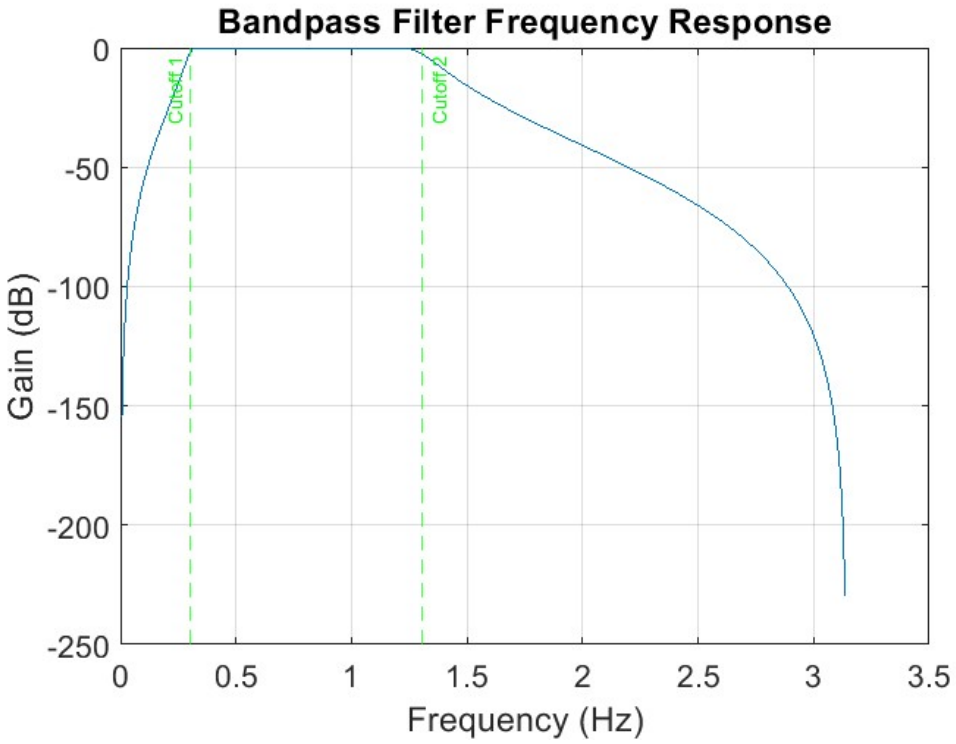

Figure 2.3: Frequency response of a Band-Pass Filter

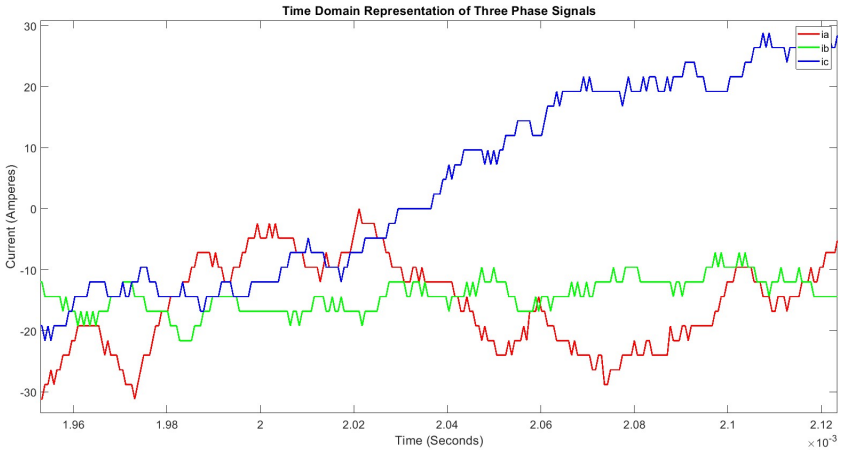

Figure 2.4: Digitization noise in a measured signal

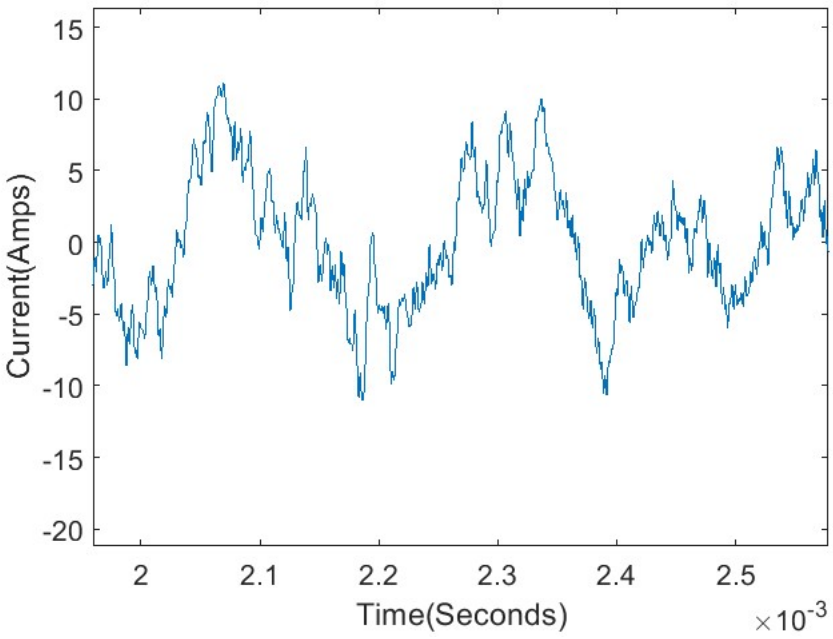

Figure 2.5: Digitization noise cleared from a measured signal by Band-Pass Filter

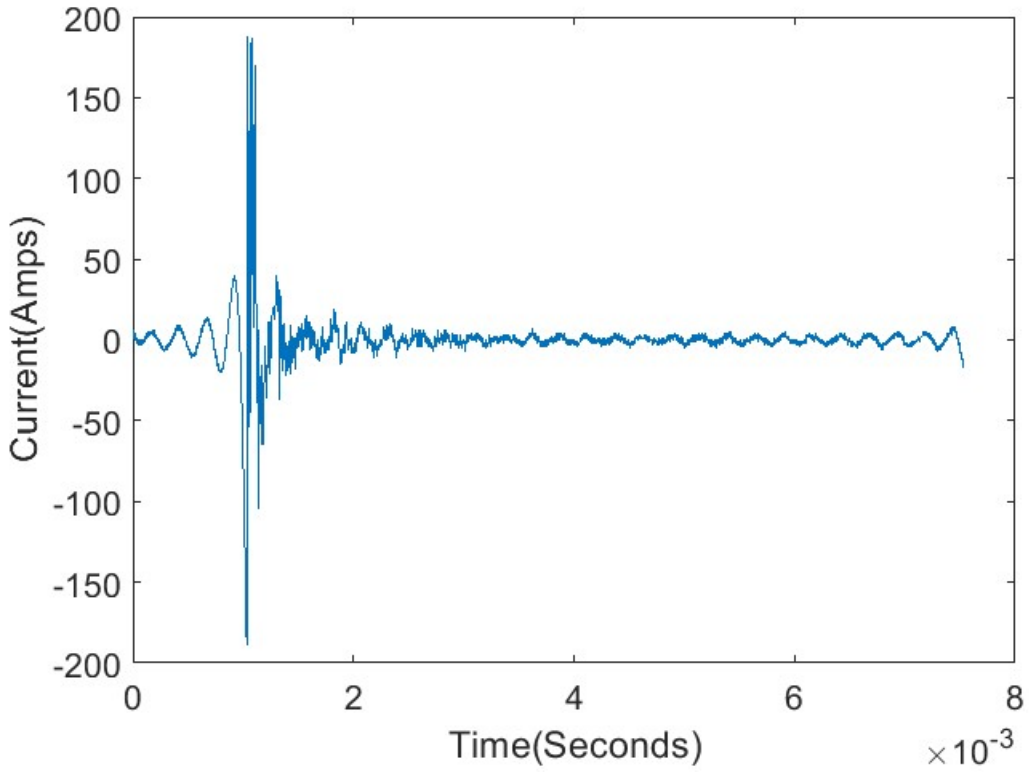

Figure 2.6: System Level Frequency Components cleared from a measured signal by Band-Pass Filter

2.3 Modular Transformation

Clarke Transformation [42] is an essential step in conditioning the signal for the fault location process implemented in this research. This avoids the inaccuracies resulting from mutual coupling of the transmission lines and their superpositin [32], to ensure the reliability of the detection. Clarke's Transformation of measured signals for a three-phase system is represented as follows:

$$\begin{bmatrix} I_0 \\ I_\alpha \\ I_\beta \end{bmatrix} = \frac{1}{\sqrt{3}} \begin{bmatrix} 1 & 1 & 1 \\ \sqrt{2} & -\frac{1}{\sqrt{2}} & -\frac{1}{\sqrt{2}} \\ 0 & \frac{\sqrt{3}}{\sqrt{2}} & -\frac{\sqrt{3}}{\sqrt{2}} \end{bmatrix} \cdot \begin{bmatrix} I_a \\ I_b \\ I_c \end{bmatrix} \tag{2.1}$$

2.4 MRA Analysis

After conditioning the signal and leaving out system frequency level and digitization-related frequency components, different wavelet types are employed for conducting an MRA analysis as described in Section 1.2.2. Note that the goal of decomposing the signal into its wavelet components is not compression of the signal. Therefore, every node of this MRA tree is important for the investigation. Two aspects should be considered when walking from one node to another:

1. As we climb down the tree branches or go higher on the node level, we get more specifically focused on smaller bits of frequency ranges to look for our traveling wave. We need to be on the lookout for the presence of significantly strong energy-level MOs that recur throughout the signal.
2. However, going higher in the node level would mean more down-sampling in the studied time domain signal. This becomes important when we are dealing with

lower sampling frequencies. As we lose time data-point to down-sampling, our time uncertainty increases based on the time-frequency uncertainty principle formulated in 1.8.

3. The fault location is mainly dependent on the time distance between two detected traveling waves that are propagating with the speed of light. So, every time point that we miss is interpreted as mile uncertainty in fault location equivalent to the distance that light could have traveled during that time. In other words we can translate the uncertainty introduced to fault location by losing each time datapoint as:

$$d_{uncertainty} = c\frac{dp_{uncertainty}}{F_s} \tag{2.2}$$

where $d_{uncertainty}$ is the uncertainty in the distance estimation, $dp_{uncertainty}$ is the uncertainty in datapoints, F_s is sampling frequency, and c is the speed of light. Therefore, when the fault location is close to the measurement unit, every time point counts, and we can only afford to go higher on the node level if our sampling frequency is reliably high. Analyzing the data at the node level of n would translate to $2^n - 1$ data point uncertainty.

Figure 2.7 shows a sample decomposition of the conditioned signal in 2.6. On the left-hand side and data contents of node 4 on the right-hand side. Node 4 is in the position of $(2, 1)$ in the MRA tree. This means that we have two stages of down-sampling to get to level 2 of the tree for the decomposed signal. The first thing to note is that the calculated fault distance is prone to 3 data points of uncertainty for this case. Let's take an example case where we have the sampling frequency of $1.56MHz$ for the main decomposed signal. The uncertainty for calculated fault distances at this level is calculated as follows:

$$d_{uncertainty} = 1.86 \times 10^5 \times \frac{3}{1.56 \times 10^6} = 0.36\ miles^1 \tag{2.3}$$

[1]We have used significant figures of 2 due to the high degree of uncertainty in the calculations involved. This allows us to work with readable numbers and still presents a highly sufficient level of accuracy for the application

Another important piece of information that we need to bear in mind throughout our study of the MOs in node (a, b) is that the major frequencies captured in this node belong to the frequency range of $[\frac{b \times F_s}{2^a}, \frac{(b+1) \times F_s}{2^a}]$.

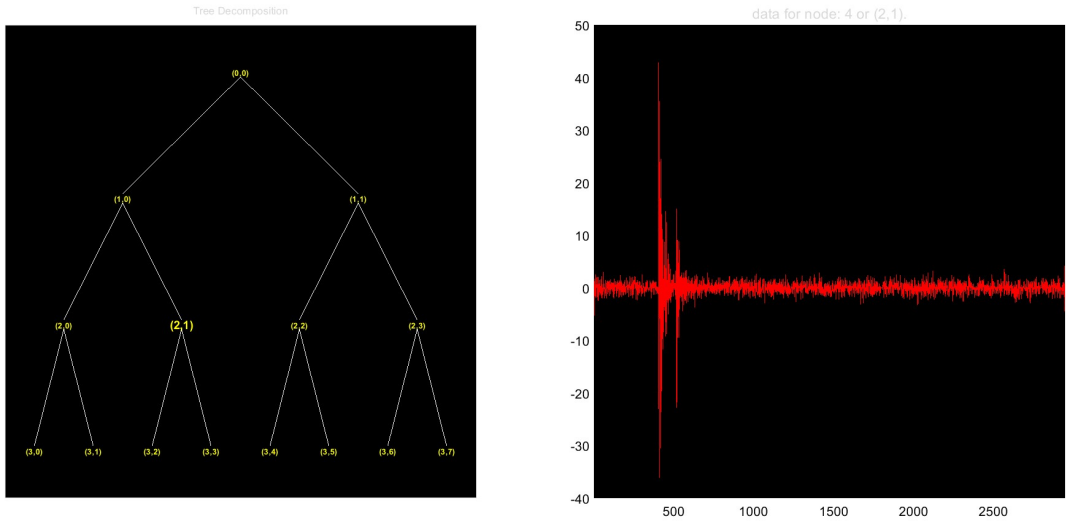

Figure 2.7: Sample Wavelet Packet Tree with db4 employed as decomposition wavelet with contents of node 4

We have employed 43 wavelets for MRA analysis and MO detection in this research. Here is a list of these wavelets:

- **Daubechies Family:** db1,db2,db3, db4,db5, db6, db7, db8, db9, and db10
- **Symlets Family:** sym2, sym3, sym4, sym5, sym6, sym7, and sym8
- **Coiflets Family:** coif1, coif2, coif3, coif4, and coif5
- **Fejér-Korovkin Family:** fk4, fk6, fk8, fk14, fk18, and fk22
- **Biorthognal Family:** bior1.1, bior1.3, bior1.5, bior2.2, bior2.4, bior2.6, bior2.8, bior3.1, bior3.3, bior3.5, bior3.7, bior3.9, bior4.4, bior5.5, and bior6.8

The implemented wavelet types manifest diverse characteristics such as orthogonality, smoothness, localization, vanishing moments, symmetry, number of coefficients, and

filter length [39]. For example, Daubechies, symlets, and biorthogonal filters, each showcases unique traits that influence their utility in signal processing. Daubechies filters are well-known for their compactness, providing the shortest filter length for specific frequency separation needs, making them highly efficient in scenarios where minimizing computational resources is vital. Symlets, akin to Daubechies, prioritize compactness but also emphasize symmetry in their design, enhancing performance for certain signals by ensuring a more balanced representation between time and frequency domains.

In contrast, biorthogonal filters stand out due to their symmetry—a rare quality among wavelet families. This symmetry allows them to preserve signal shape post-down-sampling, crucial for maintaining vital signal characteristics. This attribute is particularly beneficial for accurate signal reconstruction after down-sampling, preventing distortion of essential signal elements. As a result, biorthogonal filters are anticipated to excel in down-sampling processes due to their capacity to maintain signal shape, enhancing the accuracy of the down-scaled signal.

However, in dealing with stochastic signals characterized by unpredictability, determining the dominant filter features becomes challenging. The unpredictability of stochastic signals raises uncertainties about which specific characteristics of wavelet filters best capture signal properties. In such cases, the focus shifts from individual filter superiority to seeking consensus among the varied attributes of wavelet families. The aim becomes finding a combination of these diverse characteristics to accurately represent stochastic signals.

2.5 Segmentation

Once the signal is pre-processed in MRA tree, the data in the nodes of interest are ready to be studied in terms of strong bursts of energy *i.e*. Measurement Occurrences (MOs) inside them. In this project, we have developed an easy-to-tune segmentation algorithm that scans the normalized signal recursively and makes the decision to categorize each data-point as: (a) it is start of a new MO, (b) it is continuation of a previously started MO, (c) it is ending point of a previously started MO, (d) it is an insignificant data-point between MOs.

In this section, we delve into the logical flow of this segmentation tool for making decisions about each data-point of the segmented signal. A block diagram of the designed Segmentor's inputs and outputs is shown in figure 2.8. We refer to Amplitude Threshold, Patience Factor, Minimum Length, Tail Threshold, and Tail Patience as *Segmentation Configuration*. Let's take a look at the functionality of each of these parameters:

- **Amplitude Threshold:** This parameter functions as the threshold for a data-point to be considered as significant. When the value of a data point is greater than the amplitude threshold, it is more likely to be considered as the start point of an MO or the continuation of a previously started MO. However, being significant for a data point is not a guaranteed pass for it to be categorized in any of the groups, it's just a piece of information we have about the data point.
- **Patience Factor:** This parameter denotes the number of insignificant data points we tolerate for a previously started MO before marking its endpoint. Once the number of consecutive insignificant data points of a MO reaches the patience factor, we assign a temporary endpoint at the first insignificant data point that occurred in the series.

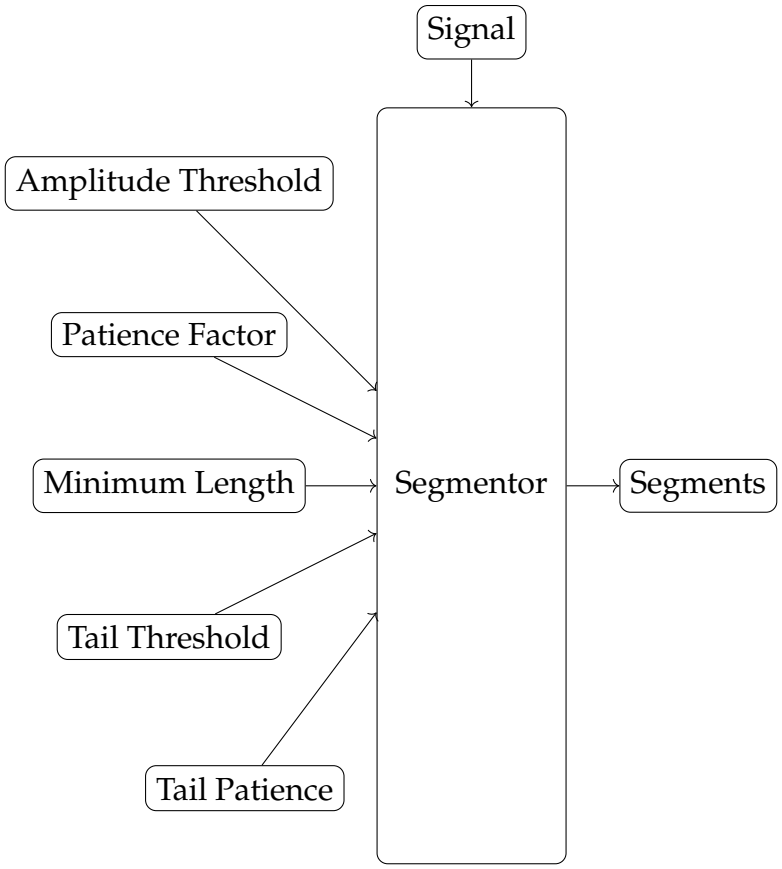

Figure 2.8: I/O Block Diagram of Designed Segmentor Process

- **Minimum Length:** This parameter is intended to prevent false peaks induced by pre-processing of the signal to be categorized as MOs. After all the MO candidates are extracted, the MOs that do not meet the minimum length criteria are marked for deletion unless they meet specific criteria to make it to the final segments list. The criteria for keeping an MO smaller than the minimum length is that its peak should be larger than a multiplier of amplitude threshold.
- **Tail Threshold:** This parameter comes into play after the first round of segmentation based on amplitude threshold and patience factor. This threshold takes a smaller value than the amplitude threshold, and its functionality is to give the insignificant data points immediately after the endpoint of an MO candidate a second chance to be considered as an extension of that MO. The insignificant data points

after the endpoint of an initially detected MO that is larger than this threshold are marked as semi-significant and are considered to be added to the recently ended MO if they meet specific criteria. This criterion is defined by the slope of the envelope of the MO from its peak to the endpoint. Adding the new data point to the end of the MO should not disrupt the MO's falling pattern by increasing the current slope of the MO's envelope. If it does, the data point will be rejected. Having more data points in an MO does not affect the maximum point of the MO and TOA; however, it makes the extracted MO larger and facilitates future frequency studies.

- **Tail Patience:** This parameter denotes the number of insignificant data points that we tolerate in the tail extension process using the tail threshold before we mark the endpoint of an MO.

The output of the Segmentor is in the format of a table, which has the MOs listed as records. The fields of each record constitute the following parameters about each segment:

1. Start Data Point
2. End Data Point
3. Start Time
4. End Time
5. Maximum Point Data Point
6. Maximum Point Time
7. MO Length

Figure 2.9 shows a sample performance of the designed Segmentor on the preprocessed signal from figure 2.7.

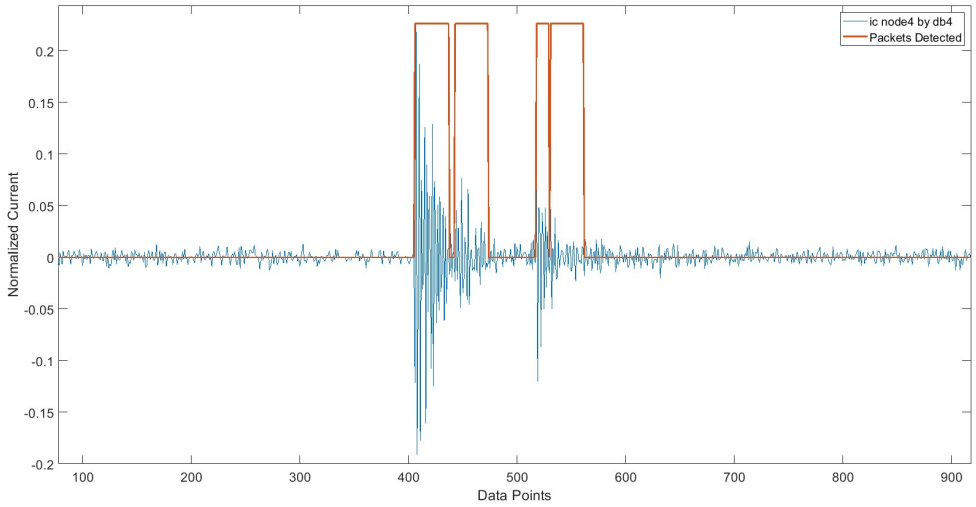

Figure 2.9: Sample Visual Output of Segmentor

2.6 Database Formation

Our algorithm employs the 43 wavelets mentioned in Section 2.4 to conduct MRA Analysis on all three phases of the measured signals and provide processed signals for the developed Segmentor to identify the MOs inside them. Each identified MO is labeled with a Unique ID (UID) for the database and following information are extracted to be stored in their respective fields:

- Phase of the measured signal
- Wavelet type used for preprocessing
- Node of the preprocessed signal in MRA tree
- Order of the MO in the detected signal
- Start data point number
- End data point number
- Start time in ms

- End time in ms
- Duration of MO in μS
- Energy level of the MO $\sum x^2$
- Pointer to time domain array of the MO
- Pointer to FFT of the MO
- General Clustering Number using K-means based on start time. The performance of this clustering is enhanced by 300 iterations after database creation
- slope of the envelope for the falling side of the MO.

2.6.1 Ensemble Voting Structure

In this chapter, we have implemented an Ensemble Voting approach to score the characteristics of the MOs detected by each wavelet type derived from the scheme proposed in [43]. Before we get to the mathematics of the approach, it is helpful to mention that the voting process is designed to simulate the social media behavior among different wavelet types. In this virtual social media, the wavelets are users. Each detected MO by that wavelet type creates a post with that user as the author detailing the characteristics of that detected MO. Each post's underlying characteristics include the MO's Start Point, End Point, and Maximum Point.

The combination of the phase or Clarkes' component and MRA tree node that yields the filtered signal for MO detection is modeled as a Hashtag/Topic in the post to facilitate the classification of the findings and comparison process. The designed social media structure allows each post to be evaluated by other non-authoring wavelet types and measure the cumulative confidence rating of the post in different aspects. The confidence

rating that each non-authoring wavelet type leaves on each post is mainly based on the personal experience of the wavelet type in that post's specific hashtag.

There two approaches that can be implemented for designing voting structure of an ensemble method:

1. Hard Voting: where the submitted vote for each aspect of the found MO is in the form of either approving (+1) or disapproving (-1) the finding based on the reviewing wavelet's experience in the post topic
2. Soft Voting: where the submitted vote is number between -1 to +1 based on the proximity of the closest experience the reviewing wavelet has regarding the topic of the found MO.

The confidence rating of each post is calculated as follows in the voting system:

$$I_{p,j}^{\omega,h} = \sum_{\gamma \neq \omega} i_{p,j}^{\gamma,h} \tag{2.4}$$

where $I_{p,j}^{\omega,h}$ is the total confidence rating of j^{th} aspect of reported MO p detected by authoring wavelet ω in the phase or Clarke's component (topic) h, and $i_{p,j}^{\gamma,h}$ is the confidence score given to the detected MO p by reviewing/non-authoring wavelet γ in its j^{th} aspect and topic h.

In the hard voting system, the confidence ratings are formulated as follows:

$$i_{p,j}^{\gamma,h} = \begin{cases} +1 & \text{if } \left| c_{m,j}^{\gamma,h} - c_{p,j}^{\omega,h} \right| < T_j \\ -1 & \text{if } \left| c_{m,j}^{\gamma,h} - c_{p,j}^{\omega,h} \right| \geq T_j \end{cases} \tag{2.5}$$

where $c_{m,j}^{\gamma,h}$ is the j^{th} characteristic of MO m detected by the reviewing wavelet γ in the topic h which is the closest to the reviewed MO p. Similarly $c_{p,j}^{\omega,h}$ is the j^{th} characteristic of

MO p detected by the authoring wavelet ω in the topic h. In other words, we can write that $\left|c_{m,j}^{\gamma,h} - c_{p,j}^{\omega,h}\right| = Min.(\left|C_j^{\gamma,h} - c_{p,j}^{\omega,h}\right|)$. $C_j^{\gamma,h}$ being the array of j^{th} characteristic of all MOs detected by reviewing wavelet γ in the topic h. T_j is the data point threshold for judging the accuracy of the post's finding based on the reviewing wavelet's experience.

In the soft voting method, instead of assigning -1 or +1 on a hard threshold, the confidence ratings are spread between -1 and +1 based on the proximity of the reviewing wavelets' experience to the characteristics of the studied MO. In other words:

$$i_{p,j}^{\gamma,h} = 2e^{-\frac{\left|c_{m,j}^{\gamma,h} - c_{p,j}^{\omega,h}\right|}{\tau_j}} - 1 \tag{2.6}$$

where τ_j is the decaying factor defining how the data point differences should translate to confidence ratings. For example Figure 2.10 represents how the confidence ratings are assigned for a $\tau = 5$. In this config, the wavelet has a positive confidence rating up to 3 point difference with the studied post, and then the confidence ratings become negative moving towards -1 as the difference increases.

2.6.2 Database Refining and Fault Location Process

In the database refining stage, for each topic (or hashtag), the entries with negative confidence ratings are removed. The percentage of removed database entries represents the overall disagreement level between different wavelet types regarding their MO detections. If the percentage of removed entries in the refining process exceeds a threshold, say 50 percent, then the results for the MO detection on that specific topic are considered inconclusive. The algorithm has a limited number of hashtags combining the aerial modes of Clarke's transformation and nodes 2, 4, and 8 of the MRA tree. However, in case of inconclusive results for all the combinations, other phases and MRA tree nodes

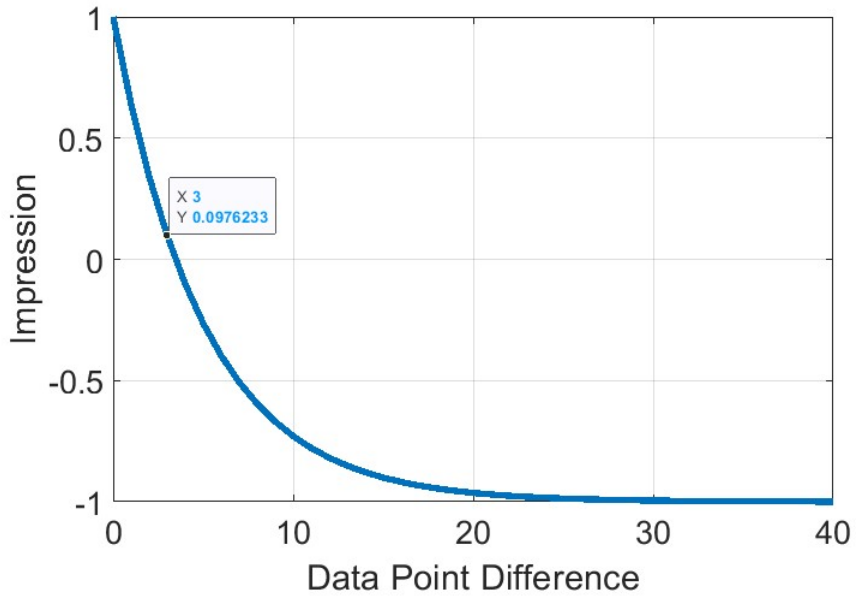

Figure 2.10: Behavior of confidence rating in a soft voting system based on the proximity of closest characteristic of found MOs by reviewing wavelet with $\tau_j = 5$

can be considered to participate in database formation.

When a hashtag meets the conclusiveness criteria the fault location database is formed based on the MOs detected on it. Fault location database entries record the essential information for the first and second MOs detected in the hashtag for each wavelet type if both MOs are not removed during the refining process. The fault location database fields for each entry includes the following information:

1. Data point for maximum point of the first MO
2. Data point for maximum point of the second MO
3. Data point Difference between the first and second MO detections
4. Time difference between first and second MO in μS
5. Mile difference between the first and second MO given the speed of propagation for the wave

After the database is formed the wave coherence of the two MOs are measured in the frequncy range of 80 kHz to 300 kHz which is the frequency range suggested in [22] for traveling waves. The wave coherence is measured using the Continuous Analytic Morlet wavelet transform modified in a concurrent research by Lawrence Durante for TW analysis purposes and following time-frequency correlation measurement approach [44]:

$$\frac{\left|S\left(C_x^*(a,b)C_y(a,b)\right)\right|^2}{S\left(|C_x(a,b)|^2\right)\cdot S\left(\left|C_y(a,b)\right|^2\right)} \tag{2.7}$$

where S is the smoothing function, $C_x(a,b)$ is the continuous transformation of signal x with scaling factor a and position factor b. Figure 2.11 shows an example matching wavelet coherence where the frequency of interest has been marked with a rectangle.

The fault location entries with an average time-frequency correlation of less than 0.5 are disqualified and removed. Then Wavelet Ensemble voting process discussed in the previous subsection scores each fault location statement based on the Mile field of the entry. The Fault location statement with the highest confidence rating is reported as the Decision of the fault location process.

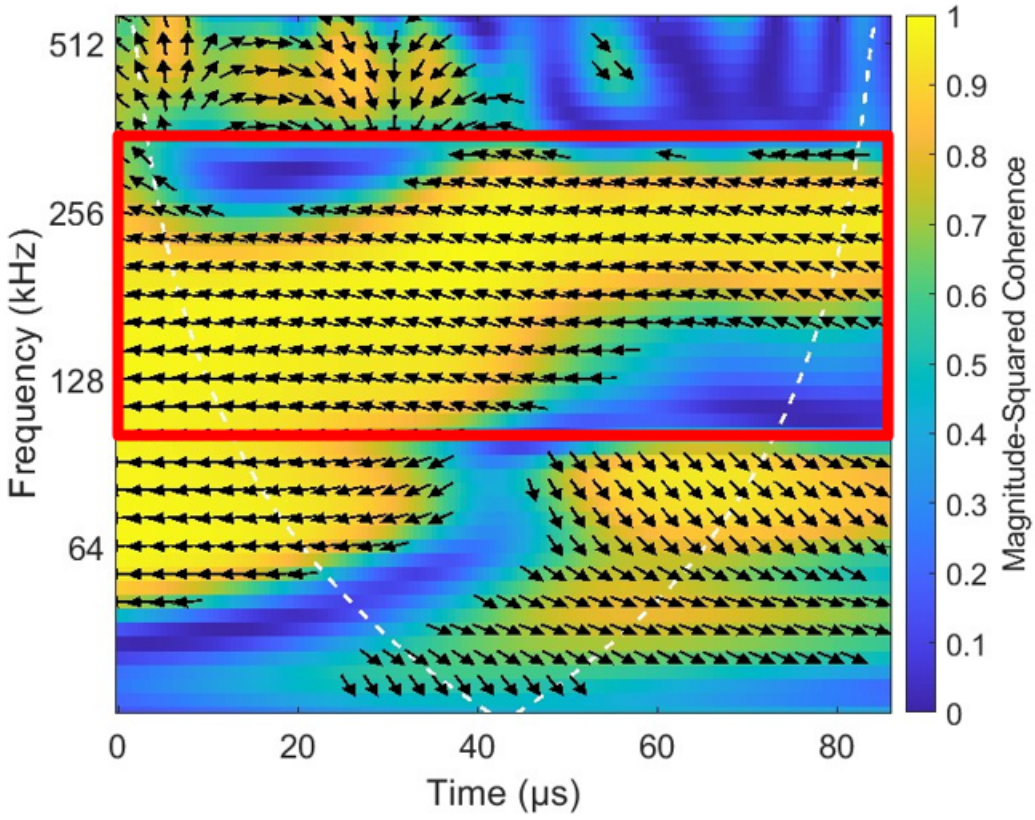

Figure 2.11: Wavelet coherence example with the frequency range of interest marked with a rectange

CHAPTER 3

IMPLEMENTATION RESULTS

We have implemented our approach on real-world measured data measured by SEL 411 L TW relays, anonymized and provided by National Grid, to detect the TW MOs and evaluate wavelet ensemble performance. The available data are measured at $1.56MHz$ in three phases for Fault and Re-close events on the same transmission line. The relay detects the discontinuity to be 8.65 miles from the measurement station.

Figure 3.1 shows the current measurements after a re-close event on a transmission line. The measurement unit for this event is situated in a substation that is 8 miles away from the next system bus. The behavior of the measured signals indicates that the re-close is successfully happening on a cleared fault. The frequency spectrum of the current signals in this event is shown in figure 3.2.

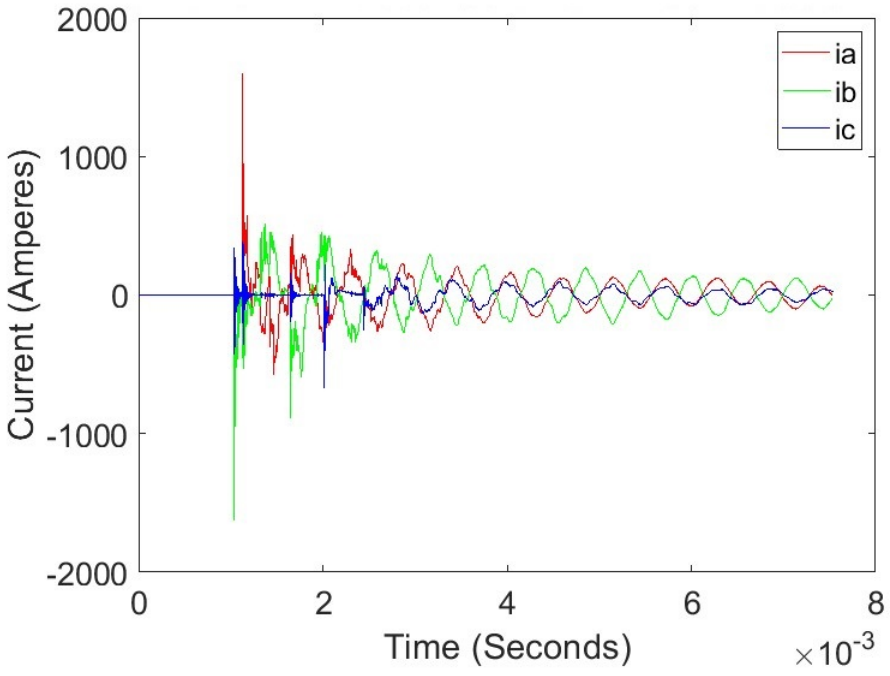

Figure 3.1: Time Domain Measurements of a Re-close Event

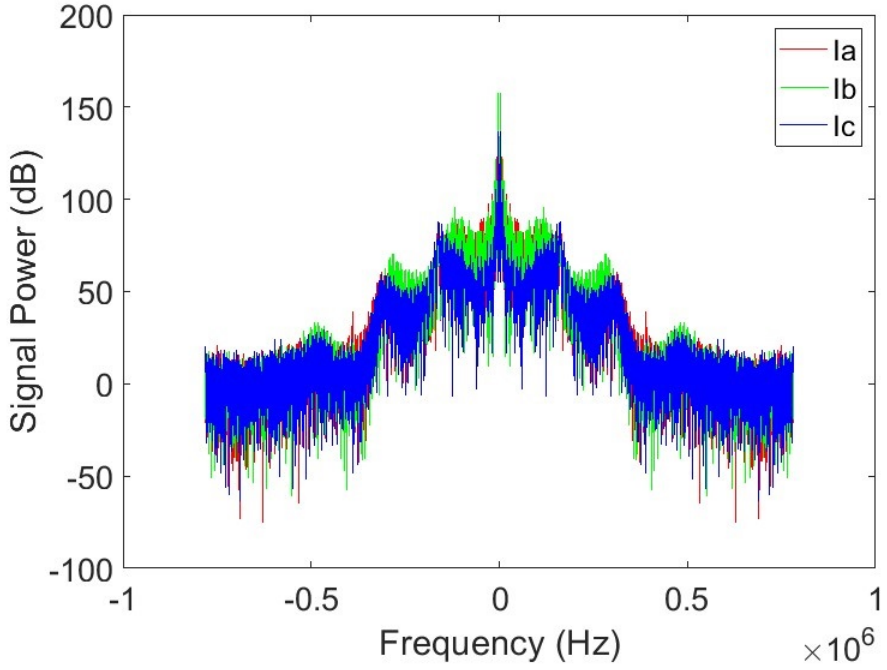

Figure 3.2: Frequency Domain Representation of Re-close Event

The extracted signals from nodes 2 , 4, and 8 of the MRA tree formed for this signal are shown in figures 3.3, 3.4, and 3.5 using db 4. As we can see, different nodes provide different levels of clarity on where the energy bursts are, and the best option can also be different for faults with different wave shapes and noise levels. The implemented algorithm switches between these 3 nodes to reach a conclusive decision on the fault point with maximum wavelet agreements. In this switching, the nodes with lower levels are prioritized to reduce the uncertainty introduced by downsampling. Figure 3.6 shows the performance of the developed Segmentor on a sample signal extracted from the MRA tree.

Table B.1 in Appendix B shows a relevant subset of the created database table for all the detected MOs by the 43 wavelets re-listed below in the studied scenario and its Clarke components.

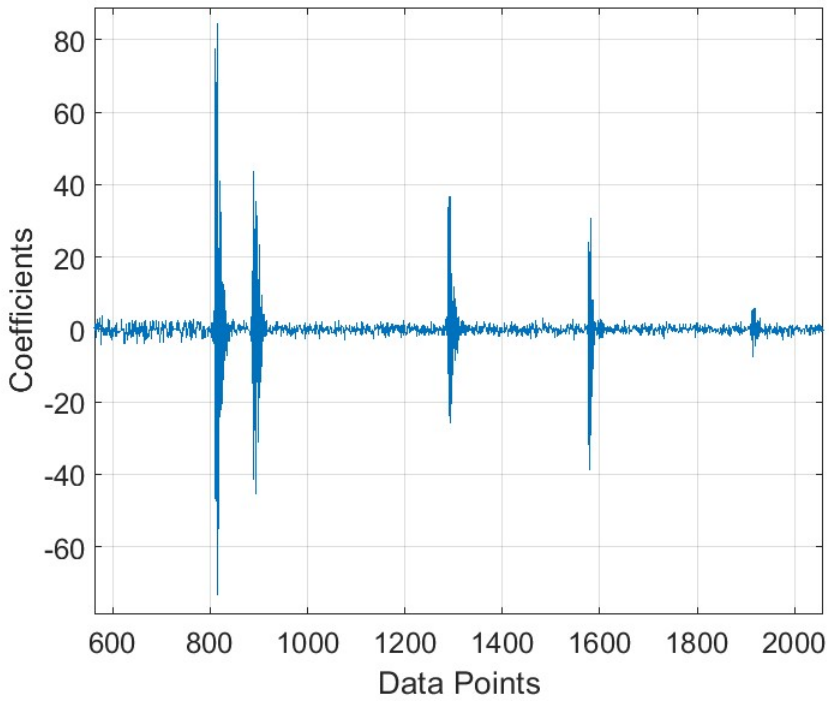

Figure 3.3: MRA result of re-close event for node 2 using db4 on alpha Clarke component

- **Daubechies Family:** db1,db2,db3, db4,db5, db6, db7, db8, db9, and db10
- **Symlets Family:** sym2, sym3, sym4, sym5, sym6, sym7, and sym8
- **Coiflets Family:** coif1, coif2, coif3, coif4, and coif5
- **Fejér-Korovkin Family:** fk4, fk6, fk8, fk14, fk18, and fk22
- **Biorthognal Family:** bior1.1, bior1.3, bior1.5, bior2.2, bior2.4, bior2.6, bior2.8, bior3.1, bior3.3, bior3.5, bior3.7, bior3.9, bior4.4, bior5.5, and bior6.8

The ensemble voting process application on the findings of this table yields the highest confidence rating arrival times that are listed in the following table.

The database refining process removes all the detected MOs with negative confidence ratings. If more than half of the detected MOs are removed in the refining process, the

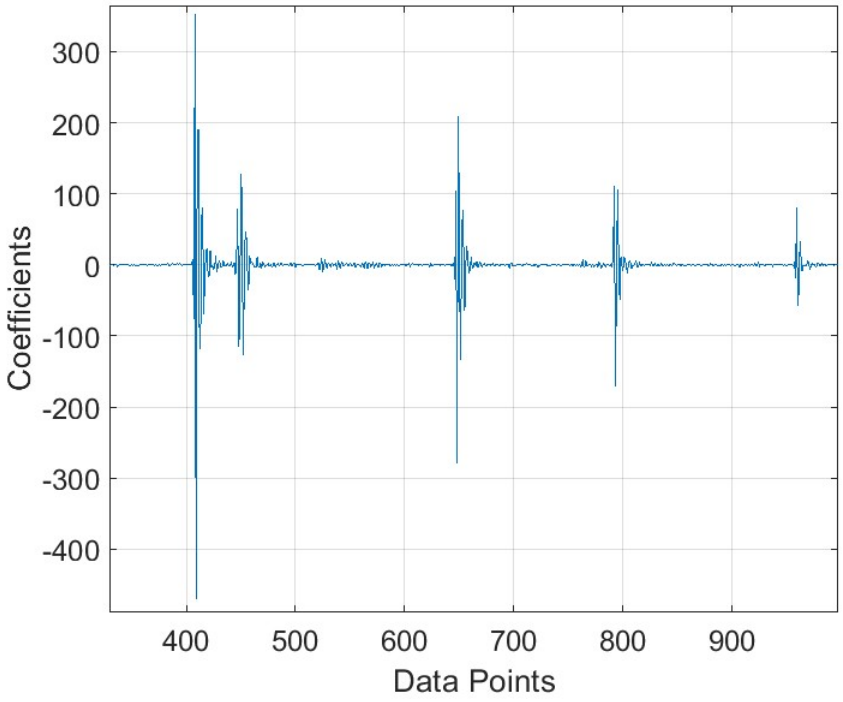

Figure 3.4: MRA result of re-close event for node 4 using db4 on alpha Clarke component

	Phase A	Phase B	Phase C	Zero Clarke	Alpha Clarke	Beta Clarke
MO 1	813	811	813	814	813	813
MO 2	885	888	890	888	886	891
MO 3	1292	1289	1292	1291	1291	1291
MO 4	1582	1581	1577	1580	1580	1578
MO 5	1915	1914	1911	1915	1912	1912

Table 3.1: Highest confidence rating Arrival Times Based on the Ensemble Voting Process

decision for the studied node will be reported as inconclusive. Then, the study automatically switches to a lower priority node on the wavelet tree, node 4. If node 4 reports inconclusive, the study will switch to node 8. The uncertainty range and probabilities change as we switch between the wavelet nodes as presented in tables 3.2. It is important to note that as we move to higher levels of the wavelet tree, the uncertainty increases. In this study node 4 has a conclusive report on the detected MOs, and the remaining

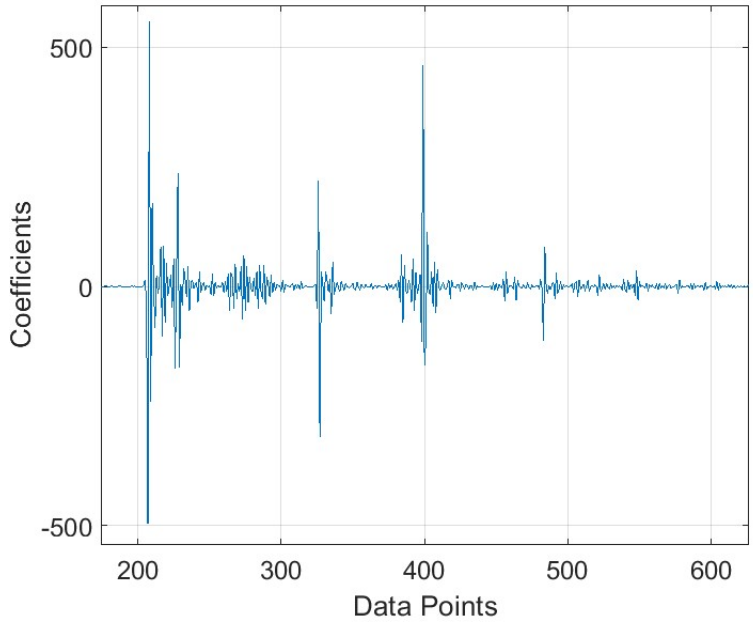

Figure 3.5: MRA result of re-close event for node 8 using db4 on alpha Clarke component

MOs with positive confidence ratings can move to form a fault location database and go through the ensemble voting process. The fault location results in the aerial mode α for this process are reported to be 8.53 miles with a 77 percent confidence rating. The top 9 fault location statements for this phase are presented in table 3.5.

The agreement level of wavelet types used for this fault location is presented in figure 3.7. In this agreement graph, wavelet types are used as nodes, and the thickness of the edges between the nodes represents the average agreement of the two wavelet types. The edges with negative weight are removed for simplification. As the agreement between multiple wavelet types increases, the graph becomes intertwined and sometimes unreadable on the agreeing side. However, the graph can be used as a tool to identify the outliers and also have a grasp of the agreement level in the obtained decision. The uncertainty and probabilities for this prediction are presented in table 3.2.

Table B.2 in Appendix B shows the ranking of different wavelet types, based on the

Uncertainty(Miles)	Probability	Interval Confidence
0	0.5	0
±0.12	0.5	1

Table 3.2: Uncertainty for detection in Node 2

Uncertainty(Miles)	Probability	Interval Confidence
0	0.25	0.25
±0.12	0.38	0.63
±0.23	0.25	0.88
±0.35	0.13	1

Table 3.3: Uncertainty for detection in Node 4

number of their appearance in highest confidence rating MOs detected in each phase. This table is sorted based on the performance of the wavelet in detecting Maximum points in the signal which denote the TOA of the traveling waves. Biorthogonal wavelets such as bior2.4 and 4.4 have shown higher consistency in detection of TOAs by contributing most to the highly approved detected MOs.

The developed method is tested on the scenario where three different Gaussian noise signals with 30 Amps are introduced to each phase. This level of noise reduces the quality of the measurement to an SNR of 6.36 dBs. Figure 3.8 shows phase A currents after introducing the Gaussian noise. The results of MO detection based on the implemented approach are shown in the table 3.6. These results show that the weaker MO5 is lost in

Uncertainty(Miles)	Probability	Interval Confidence
0	0.13	0.13
±0.12	0.22	0.34
±0.23	0.19	0.53
±0.35	0.156	0.69
±0.47	0.13	0.81
±0.59	0.09	0.91
±0.70	0.06	0.97
±0.82	0.03	1

Table 3.4: Uncertainty for detection in Node 8

Wavelet	MO1-ToA	MO2-ToA	Diff-Points	Diff μs	Miles	wcoherence	Confidence
db4	813	886	73	93.44	8.53	0.72	0.77
sym5	813	886	73	93.44	8.53	0.66	0.77
bior1.5	813	886	73	93.44	8.53	0.98	0.77
bior2.6	813	886	73	93.44	8.53	0.73	0.77
bior3.1	813	886	73	93.44	8.53	0.90	0.77
db3	812	885	73	93.44	8.53	0.63	0.77
sym3	812	885	73	93.44	8.53	0.63	0.77
bior2.4	812	885	73	93.44	8.53	0.54	0.77
bior1.3	812	885	73	93.44	8.53	0.76	0.77

Table 3.5: Top 9 Fault Location statements for reclose scenario in the aerial mode α

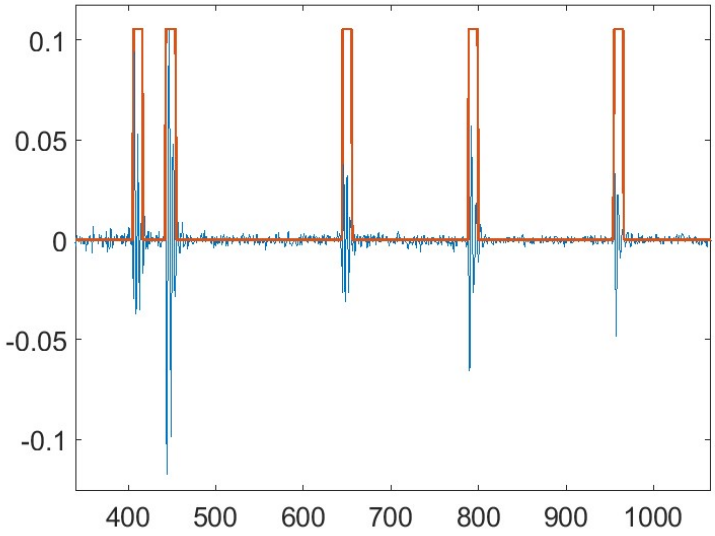

Figure 3.6: Segmentation result on a sample node of MRA tree for re-close event

the detection, as the noise has blurred it to the method. However, the main first four MOs are still detected with very close times of arrival as the original detection. The final fault location for this scenario is 8.45 miles with 63 percent confidence.

The results for fault location under different levels of noise are presented in table 3.7. This table shows that as the SNR quality of the signal drops, the detections need to be made in the lower nodes of the MRA Tree, which increases the uncertainty of the detec-

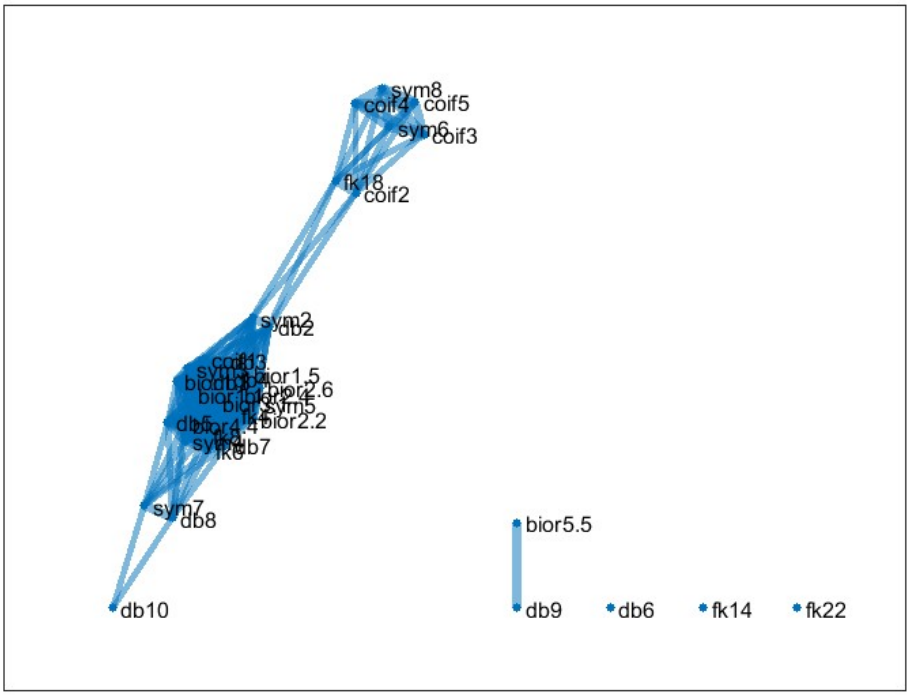

Figure 3.7: Wavelet Agreement Graph for re-close event fault location on aerial mode α

tion.

The results for fault location of 50 AMP noise are presented in table 3.8. The detections for this noise level are made at node 8 of the MRA tree with lower convergence in wavelet findings leading to a Confidence Rating of 0.26 for the top statement. Figure 3.9 shows how disagreement between different wavelet types has affected the wavelet agreement graph. However, the most prominent agreement point for wavelet types still is pointing to the fault location only with a lower confidence level.

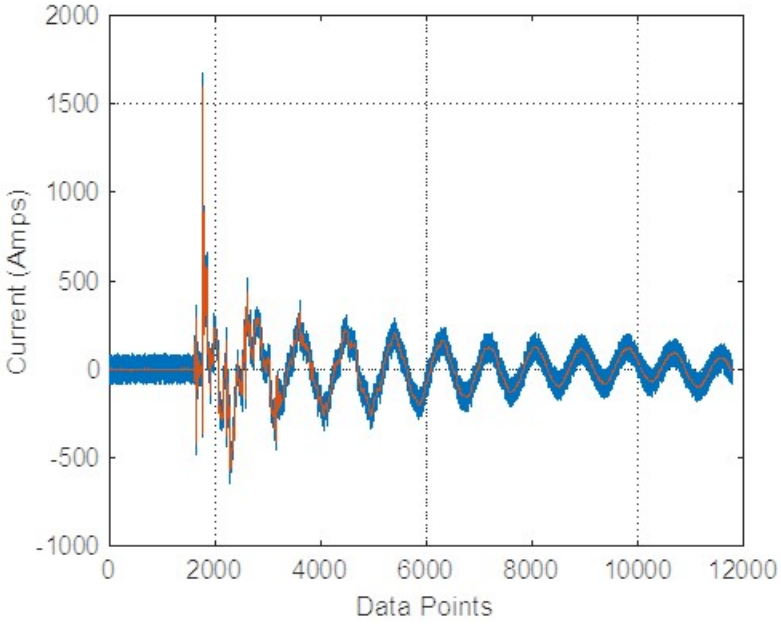

Figure 3.8: Phase A Signal after introducing 30 Amp Noise

	Phase A	Phase B	Phase C	Zero Clarke	Alpha Clarke	Beta Clarke
MO 1	813	811	813	814	813	813
MO 2	885	888	891	888	885	892
MO 3	1291	1289	1292	1293	1290	1291
MO 4	1582	1580	1577	1580	1582	1578

Table 3.6: Highest confidence rating Arrival Times Based on the ensemble voting Process after introducing a 30 Amp independent noise (SNR 6.36 dB) to each phase

Noise RMS	SNR	Fault Location	Detected Node
5	14.15	8.53	2
10	11.14	8.53	2
15	9.38	8.45	4
20	8.13	8.45	4
25	7.16	8.45	4
30	6.37	8.45	4
35	5.7	8.45	4
40	5.12	8.45	8
45	4.61	8.41	8
50	4.15	8.41	8

Table 3.7: Fault Location Results for different noise levels up to 50 Amps

Wavelet	ToA1	ToA2	Diff μs	Miles	wcoherence	Confidence
db6	207	225	92.16	8.41	0.86	0.26
bior4.4	207	225	92.16	8.41	0.5	0.26
sym6	208	226	92.16	8.41	0.44	0.26
fk14	208	226	92.16	8.41	0.61	0.26
fk8	206	224	92.16	8.41	0.81	0.26
bior1.3	205	223	92.16	8.41	0.65	0.26
sym2	204	222	92.16	8.41	0.57	0.26
fk4	204	222	92.16	8.41	0.66	0.26
db2	204	222	92.16	8.41	0.57	0.26
db3	205	224	97.28	8.88	0.87	0.25
db4	205	224	97.28	8.88	0.45	0.25
sym3	205	224	97.28	8.88	0.87	0.25
bior2.6	199	208	46.08	4.21	0.69	0.06

Table 3.8: Top Fault Location statements for 50 Amp noise scenario

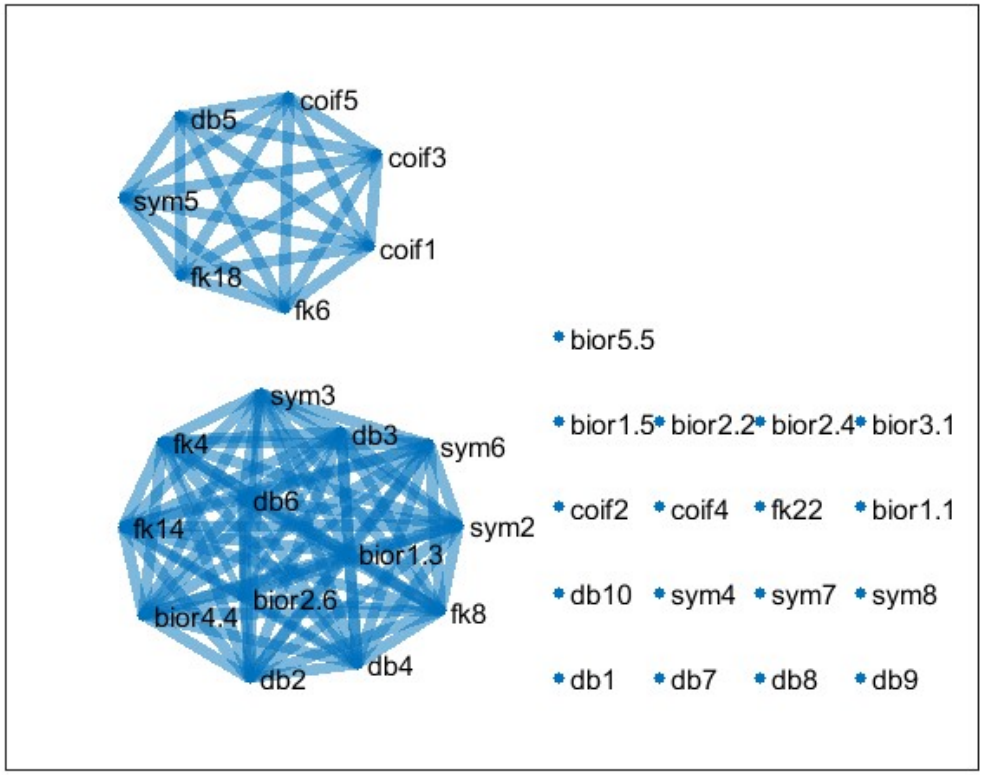

Figure 3.9: Wavelet Agreement Graph for reclose scenario with 50 Amp noise

The implemented approach is tested in a single-phase-to-ground fault scenario to assess its performance in detecting the fault-induced MOs for fault location. The data for this scenario is measured by the same relay as the previously studied scenario, SEL 411 L TW, with 1.56 MHz sampling rate. Figure 3.10 shows the three-phase currents measured for this fault. The fault location for this scenario is reported at 13.3 Miles based on the report from SEL 411 L TW Relay which has used an impedance-based method for this purpose. The previous re-close scenario has also provided the insights that two discontinuities are distanced at 8.41 Miles and 55.8 Miles from the measuring relay using the MO time points we have detected in table 3.1.

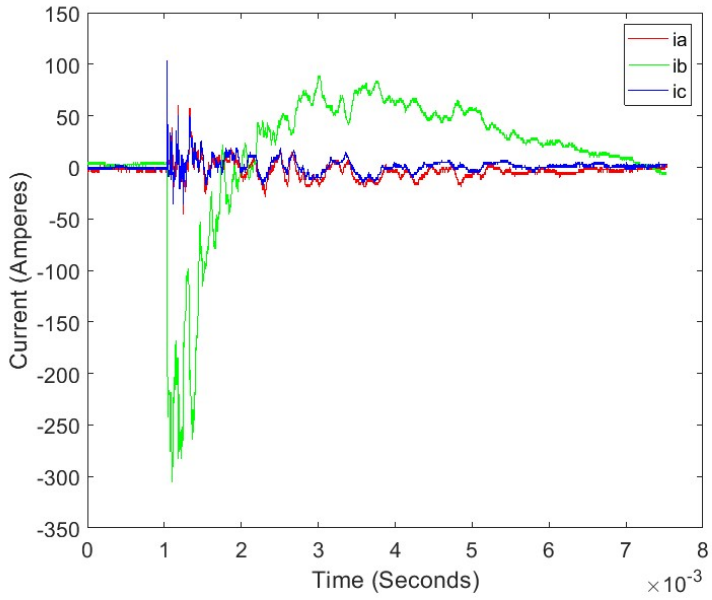

Figure 3.10: Time Domain Signals for Single Phase to Ground Fault

Clarke's transformation components are first extracted for this scenario. Figure 3.11 shows the extracted Clarke components for this fault. MRA Analysis and Segmentation process using the same set of wavelet types as the previous scenario. The database is formed with 1092 MO entries for the studied phases. A relevant subset of this database for detections on Clarke's alpha component is provided in table B.3 in Appendix B.

Wavelet Ensemble voting is implemented on the studied database. Then the refining process for each node of the MRA tree is implemented, which leads to reporting inconclusive MO findings on Node 2 and switching to Node 4 where the results are conclusive as presented in the agreement graph in figure 3.12. The thickness of the edges in this graph represents the average confidence rating between each wavelet pair. The edges for negative averages have been removed.

Fault location statements are created for the findings in Node 4. The top results for the fault location process are presented in table 3.9. The reported fault location decision for this scenario is 13.32 Miles which is very close to the 13.3 Miles reported fault location for this scenario. The uncertainty associated with this result complies with table 3.3. For single-phase to ground faults, it is important to note that multiple wave reflections hit the measurement unit following the Bewley Lattice diagram pattern in section 1.2. Therefore wave coherence checking plays a vital role in ensuring that the model converges on the fault statements with high time-frequency correlation between the first and second MOs.

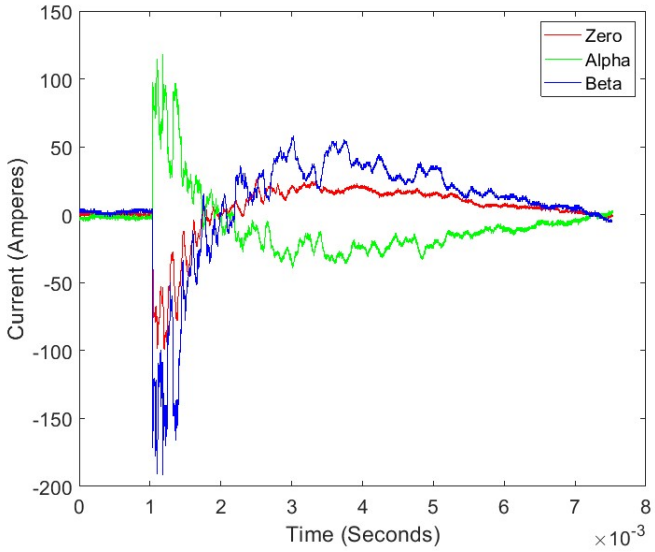

Figure 3.11: Clarke Components for Single Phase to Ground Fault Currents

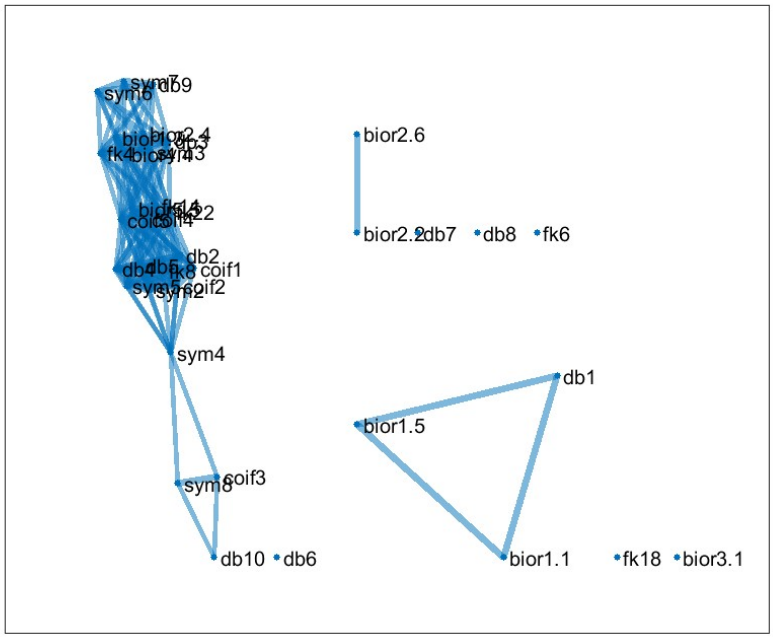

Figure 3.12: Average Confidence Rating Graph Among Wavelets in Node 4 for Single Phase to Ground Fault

	1 Wavelet	2 MO1	3 MO2	4 MOdiff	5 MOdiff	6 Mileage	7 ConfidenceRating
1	'db4'	408	465	57	145.9202	13.3197	0.4786
2	'db5'	408	465	57	145.9202	13.3197	0.4786
3	'sym5'	408	465	57	145.9202	13.3197	0.4786
4	'bior5.5'	408	466	58	148.4802	13.5534	0.4703
5	'fk14'	408	466	58	148.4802	13.5534	0.4703

Table 3.9: Top Five Fault Location Findings for Single Phase To Ground Fault Scenario

CHAPTER 4

CONCLUSION AND FUTURE WORK

In this dissertation, we have designed, implemented, and analyzed a novel method for fault location in power system transmission lines using the wavelet ensemble method. Our method utilizes different wavelet types in a cooperative algorithm to cope with the uncertainty of fault-induced wave shapes that are random, unpredictable, and non-stationary. The developed scheme is sensitive to performing the detection at the lowest uncertainty level possible. We have developed an automatic MO detection scheme that is highly adaptable and robust to help the wavelet ensemble method operate coherently without human subjectivity in fault inception reporting. We have tested the method on real-world measurements regarding re-close and single-phase-to-ground faults. The implemented method has shown accurate performance in both scenarios. We have also tested the method under heavy noise and poor SNR conditions, and the performance of the method is significantly robust to high noise levels. The developed methodology is versatile, with potential applications in a compact process unit for localized decision-making and reporting, functioning as a Relay feature. This allows for fast decision-making with lower cybersecurity risks. Alternatively, it can serve as the foundational core for a stand-alone software feature for utility operations that receives the measured data from the substation, providing more advanced visualization and documentation capabilities at the control/service dispatch center. This functionality will provide better post-processing and analysis of the situation before decision-making at the expense of higher cybersecurity infrastructure.

4.1 Future Work

In future endeavors, this work can be expanded to:

1. Application of the method to two-ended and multi-ended data situations in the case of availability of synchronized data and comparison of the approaches in terms of robustness and accuracy.
2. Application of the method to underwater and underground transmission lines. This is a much more beneficial application for the method since it is harder to investigate the faults when the lines are not visible.
3. Comprehensive discontinuity mapping using Bewley Diagram patterns and all detected MOs.
4. The wavelet ensemble approach can be implemented for accurate MO Start and End Point detection for collecting full samples of traveling waves and using them for health-check studies
5. Modulus Maxima Method can be used for reducing the down-sampling effects in fault location uncertainty.
6. In case of availability of data, the method can be checked in real-world data cases that the impedance-based method has failed to report accurate fault location to ensure the contribution.

APPENDIX A

MODEL TUNING AND TESTING FOR CHAPTER 2

In this section, we will discuss the steps for tuning and testing our model on generic synthesized measurement signals before using it on real-world measurements. This step is important in ensuring that our model can perform satisfactorily on detecting MOs on a generic synthesized signal with known recurring MOs introduced in a specific frequency range to the signal.

A.1 Synthesized Signal

The generic synthesized signal for testing and tuning purposes is created based on a signal developed in ELE 891 (Advanced Signal Processing instructed by Dr. Tomislav Bujanovic) course homework at Syracuse University and intended to comply with the following criteria:

- Contains components in multiple frequency ranges below and above the frequency range of the introduced MO.
- Contains high-frequency components close to MO introduction times to validate the accuracy of MO detection on MRA tree nodes.
- Includes discontinuities of significant magnitude in a different frequency level, to ensure that the approach can bypass the detection of such discontinuities.

The synthesized signal for this process is constructed in sampling frequency of 1 MHz in following steps:

1. The base of the signal is formed as shown in Figure A.1 by augmenting 6 segments with following characteristics:

    - Polynomial x^4 shown in black color
    - Polynomial $ax^2 + bx$ shown in red color
    - Sinusoids with very low frequencies,$1/2\pi F_s$, approximating lines shown in blue and green.
    - The last two segments are the mirrored curves of the first two polynomials

    This signal has a significant discontinuity at the center data point which lies between the Third and the Fourth segment of the curve.

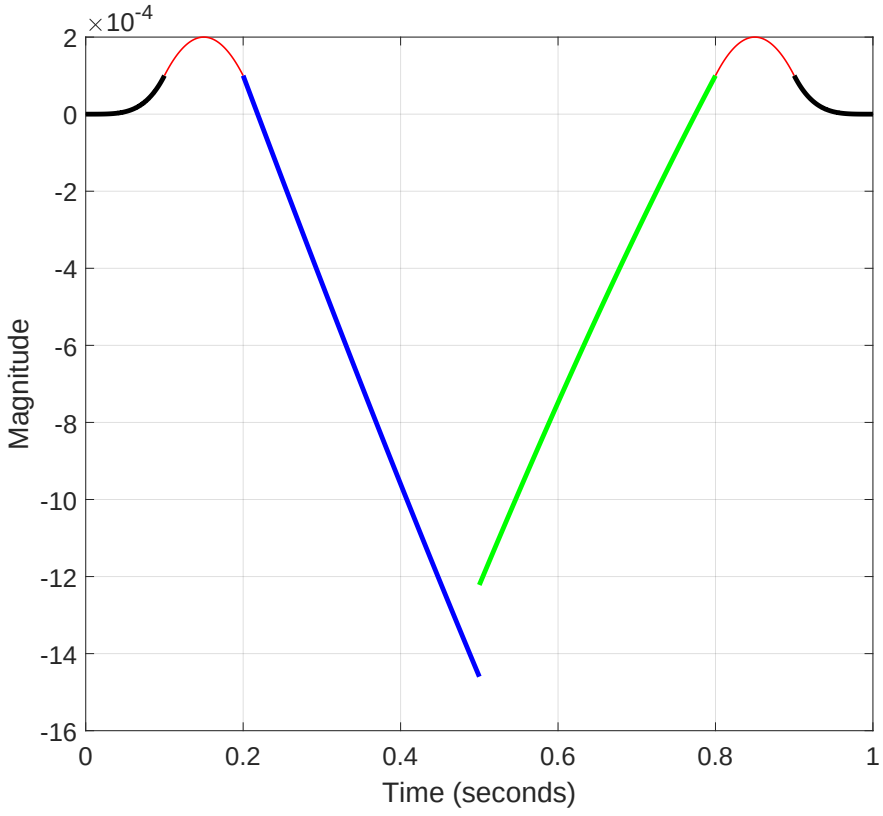

Figure A.1: Base of the synthesized signal comprised of 6 segments

2. White Gaussian noise is introduced to the base signal, and then the original signal is estimated using the modulus maxima method with Daubechies 10 wavelet in 7 iterations. This step is implemented to smoothen the signal and introduce mild imperfections to it at different frequency levels. Figure A.2 shows the polluted and reconstructed signal after this process. The reconstructed signal is duplicated to create the base of the measured signal for our synthesis without the TW packets as shown in Figure A.3.

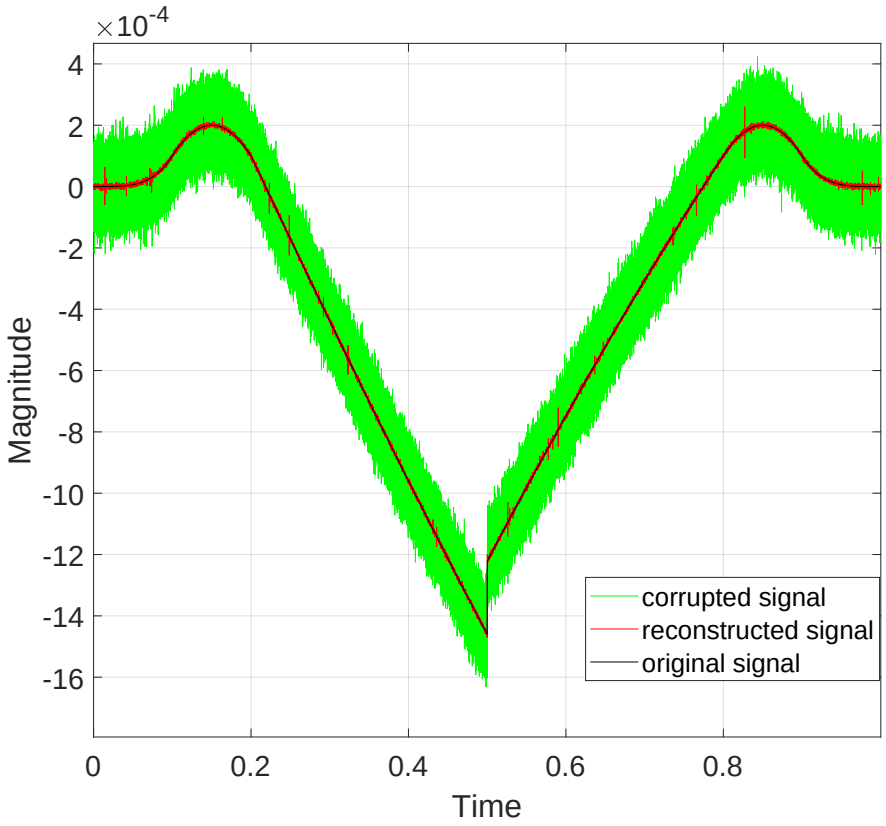

Figure A.2: Pollution and reconstruction of the base signal

3. Small bursts of energy lasting $100\mu s$ with frequency components of $f_1 = 200kHz$ and $f_2 = 100kHz$ and $f_3 = 50kHz$ are added centered to time points $0.3s$ and $0.8s$. The waves follow this equation:

$$TW = (A_1 sin(2\pi f_1) + A_2 cos(2\pi f_2) + A_3 sin(2\pi f_3))e^{-t/\tau} \tag{A.1}$$

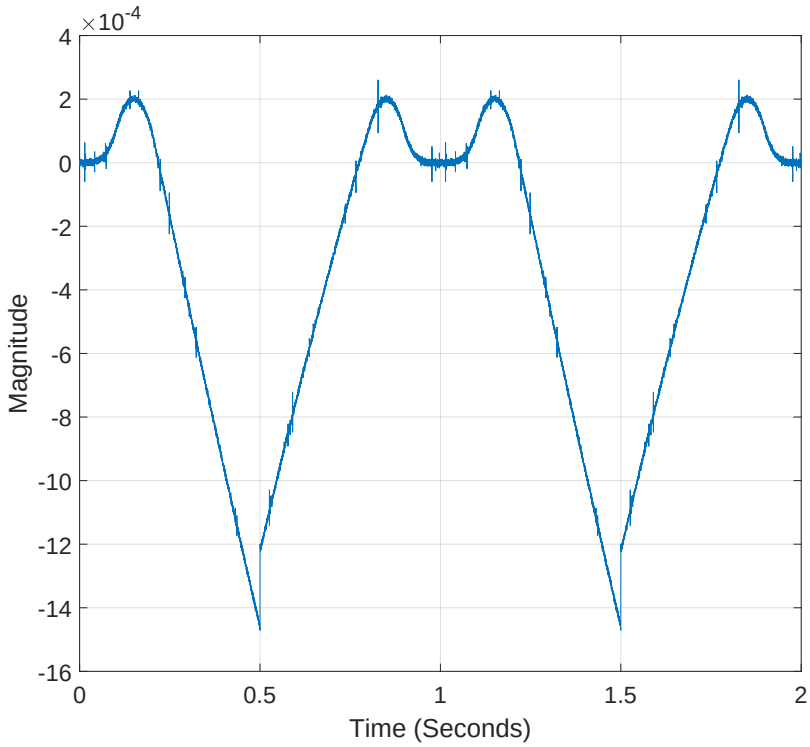

Figure A.3: Measurement base signal without TW components

Figure A.4 shows the synthesized TW packet, and Figure A.5 depicts the final measured signal with TW components added at $0.3s$ and $0.8s$.

4. White Gaussian noise is introduced to the signal to test the performance of the signal at different SNR levels. Figure A.9 shows the noisy signal with SNR of 21.52.

Based on the frequency components of the TW signal and the sampling frequency of the measured signal, the nodes of priority for detecting the arrival times of this component on the measured signal are Node 4 (sweeping frequencies between $125 - 250kHz$), Node 10 ($187 - 250kHz$), and Node 8 ($62 - 125kHz$) of the MRA tree. Figure A.6. As shown in the figure, the highest coefficients at this node occur close to 0.3 S and 0.8 S which is where we have introduced the TW components in the signal, with an exact difference of 0.5 seconds. Our goal is to find this time difference between the two maximums, as it is the base for fault location after detection by the Segmentation method introduced in

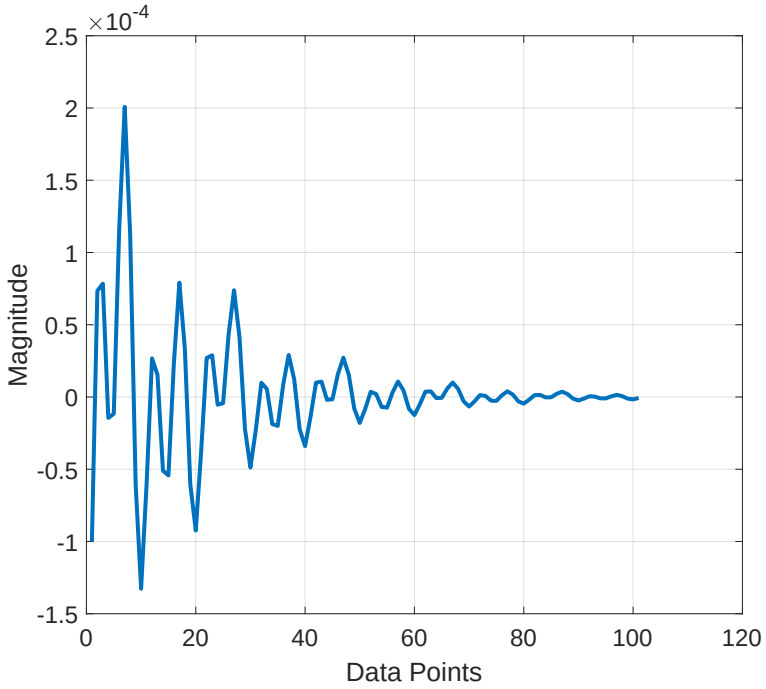

Figure A.4: Introduced TW Component

Section 2.5.

The Segmentor needs tuning to detect a reasonable number of energy bursts as well as their local maximums in the studied node to be used for fault location. For this purpose, we have developed a secondary toolbox that starts with an amplitude threshold of 1, and reduces it gradually with an initial threshold step of 0.05 while checking the number of detections in each iteration. If the number of detections exceeds the maximum number of expected detections after a specific step, the algorithm will start increasing the threshold in smaller steps. This iteration continues until the expected number of detections is reached. The segmentation algorithm adjusts the amplitude threshold in each iteration to meet the expected number of detections and finally reports the final threshold that meets the expected criteria.

For example, for the specific case shown in figure A.6, using amplitude threshoshold of 0.95, patience factor of 2 data points, and tail threshold of 0.65, the detections shown

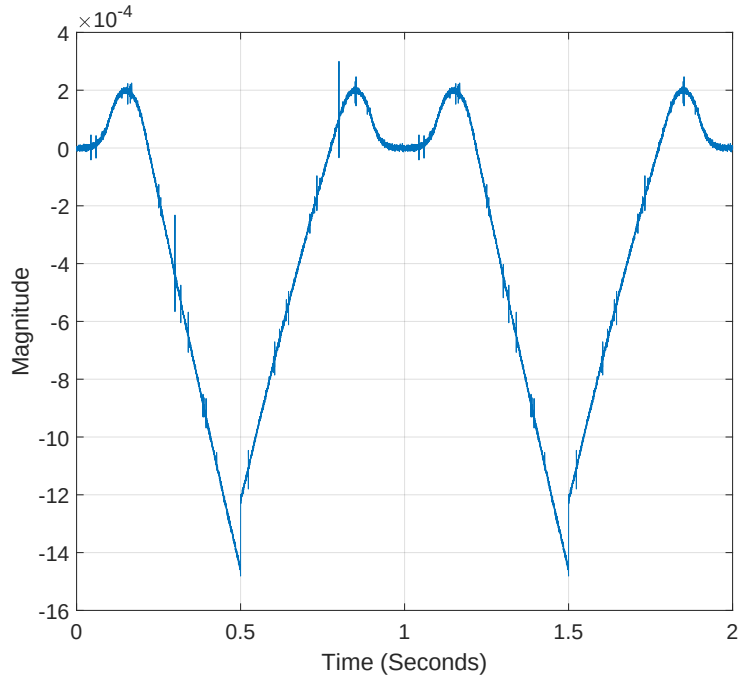

Figure A.5: Final synthesized signals after adding TW components at $0.3s$ and $0.8s$

in Figure A.7. This simple scenario shows that the segementation process successufully detects the introduced TWs in the studied signal. The wavelet filter length causes slight difference in detection times of the introduced TWs, but the distance of the two detections should stay the same as they both experience similar shifting and scaling caused by the used wavelet filter.

Running The the database formation and ensemble voting on the clean signal yields a unanimous time difference detection of 0.5 s which is the intended time difference. Figure A.8 shows the unanimous agreement of all wavelets to the time difference between the two detections.

To test the robustness of the test, White Gaussian noise is introduced to the studied signal resulting in the the signal shown in Figure A.9. The SNR of the noisy signal is calculated to be 21.56 dB. The Node 4 coefficients of this signal are shown in Figure A.10.

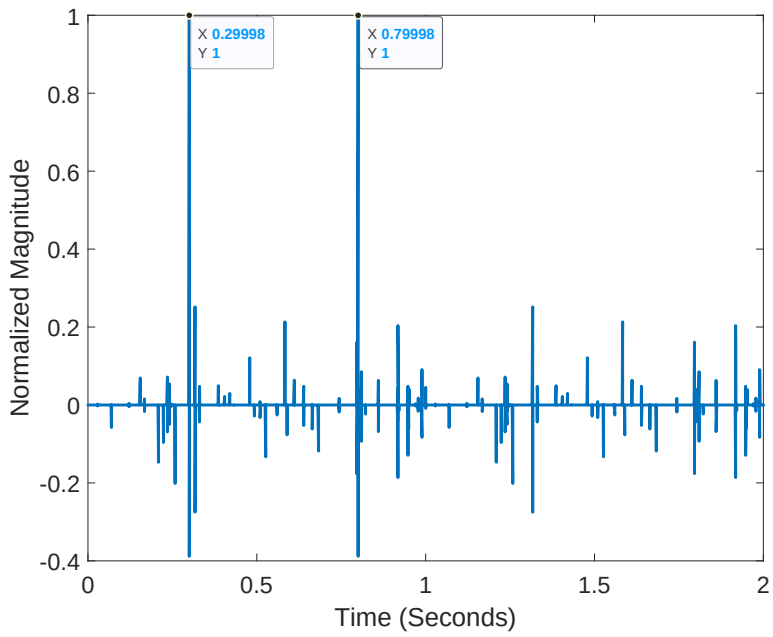

Figure A.6: Normalized node 4 components of synthesized signal decomposed using wavelet *bior*6.8

This figure shows that the noise components have a significant magnitude in node 4 of this detection. However, with fine-tuning capability of the Segmentor algorithm, the first two maximums can still be detected. In this scenario, we need to enforce a higher Tail Threshold and lower patience factor, in comparison to the clean signal scenario to avoid potential merging of the two separate segments due to noise components being present at almost every time point in between. Figure A.11 shows that with an amplitude threshold 0.938, patience factor 1, and tail threshold 0.8, the same representatives of the introduced TWs can be detected at the same location and correct time distance.

However, this approach does not yield similar results for all the wavelet types. Wavelets, depending on their filter shape and characteristics accentuate different components present in the studied signal. For example, Figure A.12 shows the coefficients and segmentation output for the first four prominent components in this node. The segmentation configuration for this scenario is similar to the configuration for the bior6.8

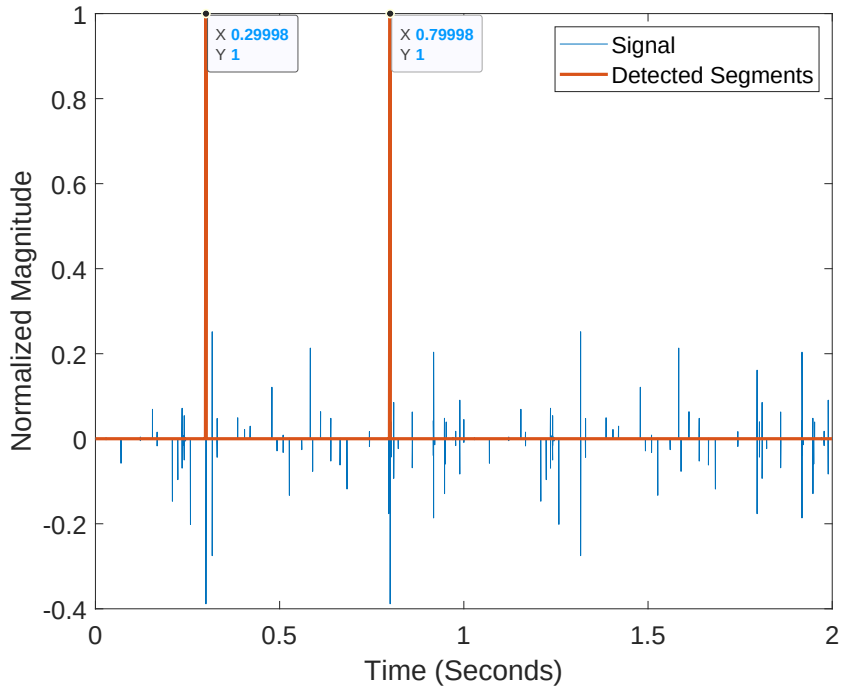

Figure A.7: Segmentation results for node 4 components of synthesized signal decomposed using wavelet *bior*6.8

case. As we can see, none of the identified components are relevant to the introduced TWs, and the time difference between them is not representative of the time difference between the two introduced TWs (0.5 s).

The database of all detections by the wavelets introduced in Chapter 3 is formed for this scenario and fault location statements are formed for node 4. Figure A.13 shows the wavelet agreement graph for this analysis. The thickness of the edges in this graph represents the average confidence rating between each wavelet pair. The edges for negative averages suggesting disagreements, have been removed for readability purposes. This graph suggests a strong agreement of 17 wavelets on a common finding. The other wavelet types have made detections that have got confirmation with only a few or no other wavelet types.

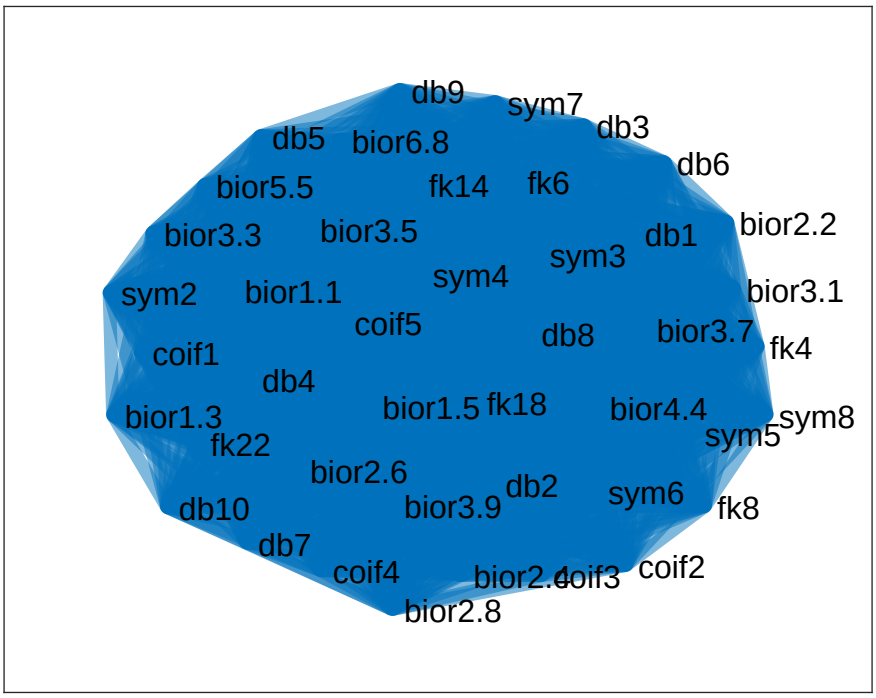

Figure A.8: Wavelet agreement graph for the clean scenario without noise

Wavelet	1^{st} Detection	2^{nd} Detection	Data Point Diff	Time Diff (ms)
fk14	74993	199993	125000	500
bior5.5	74993	199993	125000	500
db5	74992	199992	125000	500
bior3.3	74992	199992	125000	500
sym7	74994	199994	125000	500
fk18	74994	199994	125000	500
fk8	74991	199991	125000	500
fk22	74995	199995	125000	500
bior3.7	74995	199995	125000	500

Table A.1: Top 9 high-rated detection results for noisy scenario

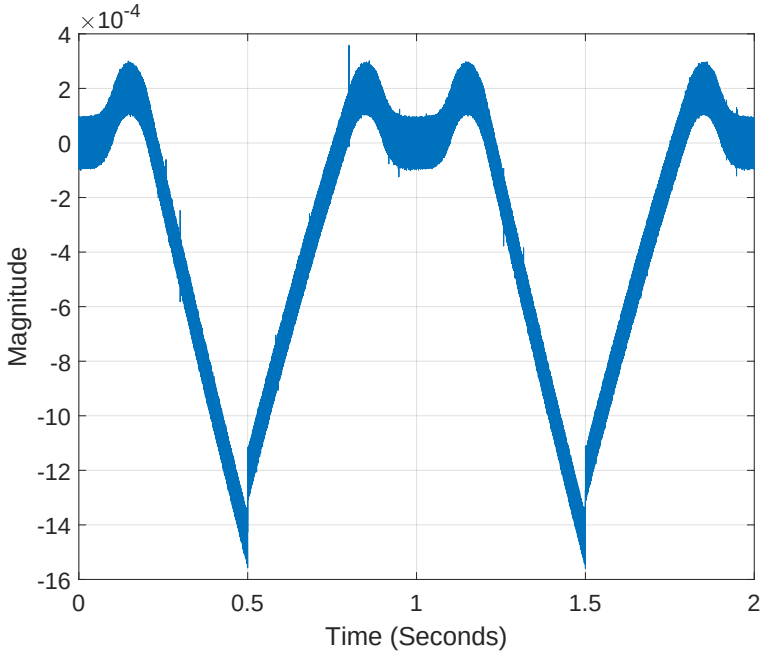

Figure A.9: Noisy Signal with SNR of 21dB

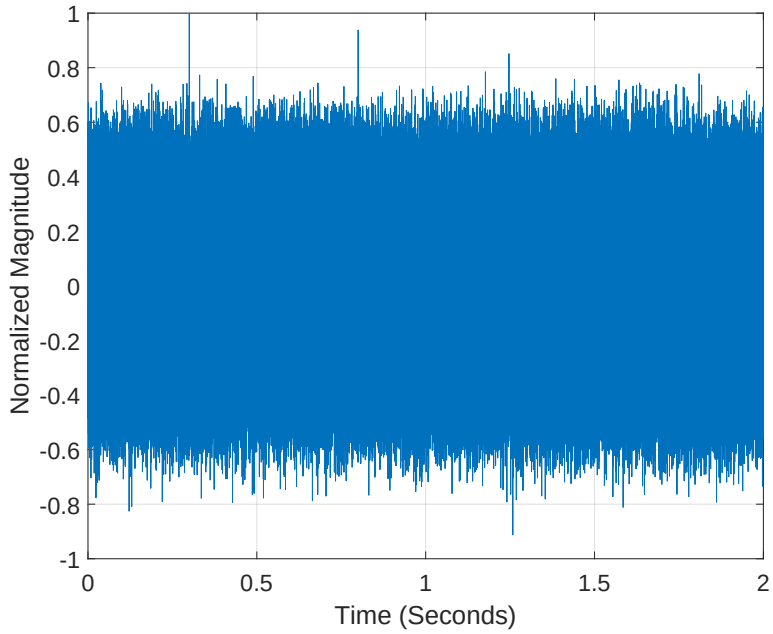

Figure A.10: Node 4 components noisy signal decomposed by *bior*6.8

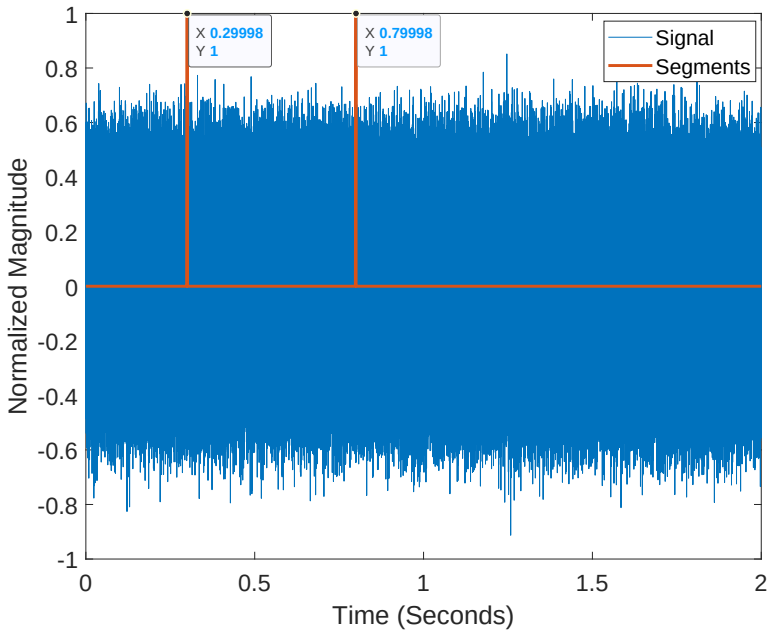

Figure A.11: Segementation result of node 4 components for noisy signal decomposed by *bior*6.8

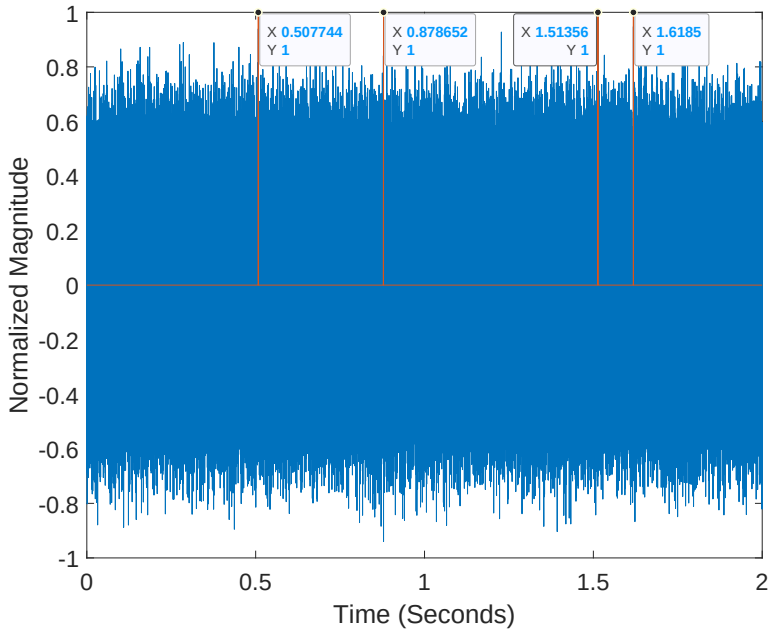

Figure A.12: Segementation result of node 4 components for noisy signal decomposed by *db*7

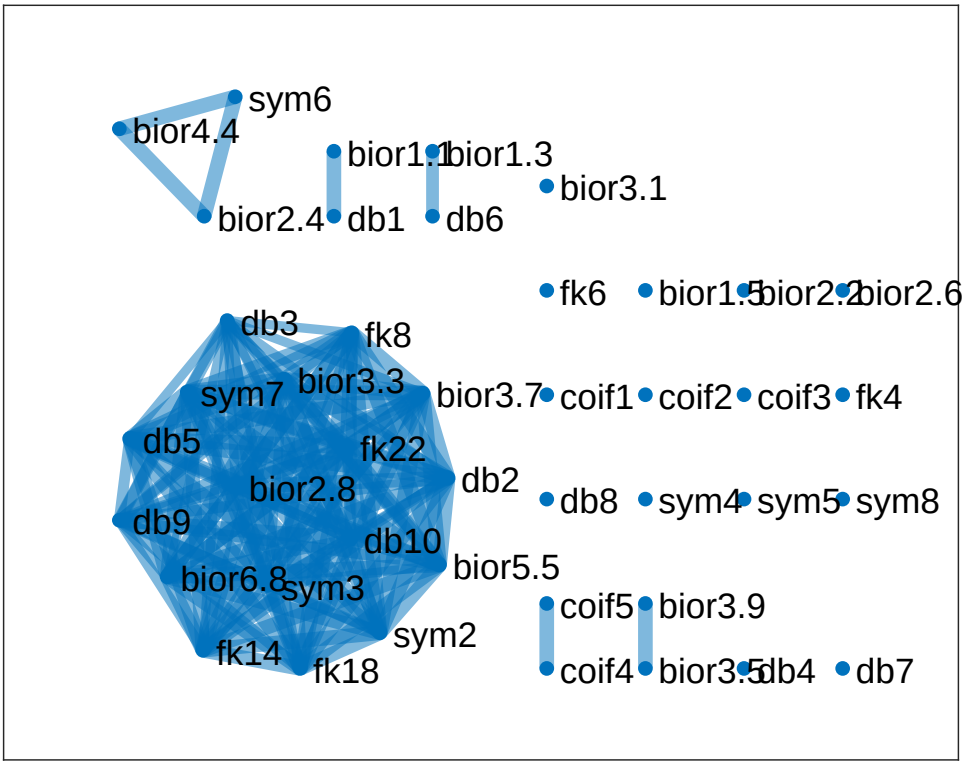

Figure A.13: Wavelet agreement graph for the noisy scenario with SNR 21.56

APPENDIX B

TABLES FOR CHAPTER 3

1 Uid	2 sigid	3 Packetno	4 Startpoint	5 Endpoint	6 Length	7 StartTime ms	8 EndTime ms	9 Duration usec	10 MaxPoint	11 Maxpoint ms	12 Energy
1	1	1	809	837	29	1.0355	1.0714	37.1201	811	1.0381	6.9482e – 04
2	1	2	884	913	30	1.1315	1.1686	38.4001	884	1.1315	0.0023
3	1	3	921	949	29	1.1789	1.2147	37.1201	922	1.1802	$3.0003e-05$
4	1	4	1112	1140	29	1.4234	1.4592	37.1201	1113	1.4246	5.4811e – 05
5	1	5	1287	1315	29	1.6474	1.6832	37.1201	1289	1.6499	$2.0607e-04$
6	1	6	1576	1604	29	2.0173	2.0531	37.1201	1579	2.0211	1.0480e – 04
7	2	1	809	840	32	1.0355	1.0752	40.9601	812	1.0394	0.0014
8	2	2	884	914	31	1.1315	1.1699	39.6801	885	1.1328	0.0034
9	2	3	1115	1145	31	1.4272	1.4656	39.6801	1115	1.4272	2.4476e – 05
10	2	4	1287	1300	14	1.6474	1.6640	17.9201	1290	1.6512	3.6227e – 04
11	2	5	1302	1332	31	1.6666	1.7050	39.6801	1308	1.6742	4.6676e – 05
12	2	6	1577	1607	31	2.0186	2.0570	39.6801	1582	2.0250	1.9024e – 04
13	3	1	809	857	49	1.0355	1.0970	62.7202	813	1.0406	0.0013
14	3	2	883	930	48	1.1302	1.1904	61.4402	885	1.1328	0.0022
15	3	3	1287	1334	48	1.6474	1.7075	61.4402	1290	1.6512	5.1557e – 04
16	3	4	1577	1624	48	2.0186	2.0787	61.4402	1583	2.0262	2.0854e – 04
17	3	5	1910	1957	48	2.4448	2.5050	61.4402	1912	2.4474	4.7435e – 05
18	4	1	810	850	41	1.0368	1.0880	52.4802	813	1.0406	0.0022
19	4	2	884	925	42	1.1315	1.1840	53.7602	886	1.1341	0.0029
20	4	3	1287	1327	41	1.6474	1.6986	52.4802	1291	1.6525	0.0013
21	4	4	1576	1616	41	2.0173	2.0685	52.4802	1579	2.0211	5.9012e – 04
22	4	5	1910	1950	41	2.4448	2.4960	52.4802	1913	2.4486	1.3076e – 04

Table B.1: A relevant subset of Database entries for the analysis of reclose event using different wavelets

	1 Wavelet Type	2 Start Point Score	3 End Point Score	4 Max Point Score
1	bior2.4	4	5	11
2	bior 4.4	17	4	11
3	sym4	17	5	10
4	coif2	15	1	10
5	bior1.5	2	0	10
6	sym5	12	2	9
7	bior3.1	12	0	9
8	db2	13	5	8
9	db4	12	0	8
10	bior1.3	8	0	8
11	bior2.6	1	4	8
12	bior5.5	11	5	8
13	db7	14	3	7
14	db8	14	3	7
15	db10	16	4	7
16	sym2	13	5	7
17	db3	13	4	6
18	db6	16	1	6
19	sym3	13	5	6
20	sym7	5	8	6
21	bior3.3	5	5	6
22	db5	12	1	5
23	db9	18	2	5
24	sym6	3	5	5
25	coif3	3	5	5
26	fk18	9	0	5
27	fk22	11	0	5
28	fk8	11	8	4
29	coif1	18	4	3
30	bior2.2	20	6	3
31	bior3.5	2	7	3
32	bior3.7	0	5	3
33	fk6	10	0	2
34	fk14	10	1	2
35	bior1.1	13	1	2

Table B.2: Wavelet performance ranking table based on the implemented method for reclose scenario

1 Uid	2 sigid	3 Packetno	4 Startpoint	5 Endpoint	6 Length	7 StartTime ms	8 EndTime ms	9 Duration usec	10 Max Point	11 Maxpoint ms	12 Energy
720	149	1	404	418	15	1.0342	1.0701	38.4001	405	1.0368	0.0013
721	149	2	420	441	22	1.0752	1.1290	56.3201	428	1.0957	3.5345e – 04
722	149	3	447	457	11	1.1443	1.1699	28.1600	451	1.1546	6.6944e – 05
723	149	4	459	479	21	1.1750	1.2262	53.7601	462	1.1827	6.8493e – 04
724	149	5	499	514	16	1.2774	1.3158	40.9601	501	1.2826	4.8792e – 05
725	149	6	516	536	21	1.3210	1.3722	53.7601	519	1.3286	1.2984e – 04
726	150	1	405	412	8	1.0368	1.0547	20.4800	406	1.0394	0.0019
727	150	2	421	429	9	1.0778	1.0982	23.0400	428	1.0957	1.3825e – 04
728	150	3	462	469	8	1.1827	1.2006	20.4800	463	1.1853	4.8936e – 04
729	150	4	482	489	8	1.2339	1.2518	20.4800	485	1.2416	4.5095e – 05
730	151	1	405	416	12	1.0368	1.0650	30.7200	406	1.0394	0.0019
731	151	2	420	432	13	1.0752	1.1059	33.2800	421	1.0778	5.2018e – 04
732	151	3	464	475	12	1.1878	1.2160	30.7200	465	1.1904	7.0188e – 04
733	151	4	544	555	12	1.3926	1.4208	30.7200	545	1.3952	1.5085e – 04
734	152	1	407	415	9	1.0419	1.0624	23.0400	408	1.0445	0.0017
735	152	2	430	438	9	1.1008	1.1213	23.0400	431	1.1034	4.0192e – 04
736	152	3	463	472	10	1.1853	1.2083	25.6000	465	1.1904	0.0024
737	152	4	577	585	9	1.4771	1.4976	23.0400	579	1.4822	8.4968e – 05
738	153	1	406	419	14	1.0394	1.0726	35.8400	408	1.0445	0.0022
739	153	2	422	436	15	1.0803	1.1162	38.4001	431	1.1034	3.8284e – 04
740	153	3	464	477	14	1.1878	1.2211	35.8400	465	1.1904	7.7948e – 04
741	153	4	484	497	14	1.2390	1.2723	35.8400	488	1.2493	1.0539e – 04

Table B.3: A relevant subset of MO Database entries for the analysis of single-phase-to-ground fault on Clarke's Alpha component

BIBLIOGRAPHY

[1] F. Wilches-Bernal, A. Bidram, M. J. Reno, J. Hernandez-Alvidrez, P. Barba, B. Reimer, R. Montoya, C. Carr, and O. Lavrova, "A survey of traveling wave protection schemes in electric power systems," *IEEE Access*, vol. 9, pp. 72949–72969, 2021.

[2] B. Kroposki, B. Johnson, Y. Zhang, V. Gevorgian, P. Denholm, B.-M. Hodge, and B. Hannegan, "Achieving a 100% renewable grid: Operating electric power systems with extremely high levels of variable renewable energy," *IEEE Power and energy magazine*, vol. 15, no. 2, pp. 61–73, 2017.

[3] M. Korkali, H. Lev-Ari, and A. Abur, "Traveling-wave-based fault-location technique for transmission grids via wide-area synchronized voltage measurements," *IEEE Transactions on Power Systems*, vol. 27, no. 2, pp. 1003–1011, 2011.

[4] A. Lei, X. Dong, S. Shi, and B. Wang, "A novel current travelling wave based single-ended fault location method for locating single-phase-to-ground fault of transmission line," in *2015 50th International Universities Power Engineering Conference (UPEC)*, pp. 1–6, 2015.

[5] H. Livani and C. Y. Evrenosoglu, "A traveling wave based single-ended fault location algorithm using dwt for overhead lines combined with underground cables," in *IEEE PES General Meeting*, pp. 1–6, 2010.

[6] H. Livani and C. Y. Evrenosoglu, "A machine learning and wavelet-based fault location method for hybrid transmission lines," *IEEE Transactions on Smart Grid*, vol. 5, no. 1, pp. 51–59, 2014.

[7] T. Takagi, Y. Yamakoshi, M. Yamaura, R. Kondow, and T. Matsushima, "Development of a new type fault locator using the one-terminal voltage and current data," *IEEE Transactions on Power apparatus and systems*, no. 8, pp. 2892–2898, 1982.

[8] L. Eriksson, M. M. Saha, and G. Rockefeller, "An accurate fault locator with compensation for apparent reactance in the fault resistance resulting from remore-end infeed," *IEEE Transactions on Power Apparatus and Systems*, no. 2, pp. 423–436, 1985.

[9] T. Kawady and J. Stenzel, "A practical fault location approach for double circuit transmission lines using single end data," *IEEE transactions on power delivery*, vol. 18, no. 4, pp. 1166–1173, 2003.

[10] C. E. de Morais Pereira and L. C. Zanetta, "Fault location in transmission lines using one-terminal postfault voltage data," *IEEE Transactions on power delivery*, vol. 19, no. 2, pp. 570–575, 2004.

[11] A. Girgis, D. Hart, and W. Peterson, "A new fault location technique for two- and three-terminal lines," *IEEE Transactions on Power Delivery*, vol. 7, no. 1, pp. 98–107, 1992.

[12] J. Izykowski, R. Molag, E. Rosolowski, and M. Saha, "Accurate location of faults on power transmission lines with use of two-end unsynchronized measurements," *IEEE Transactions on Power Delivery*, vol. 21, no. 2, pp. 627–633, 2006.

[13] M. Sachdev and R. Agarwal, "A technique for estimating transmission line fault locations from digital impedance relay measurements," *IEEE Transactions on Power Delivery*, vol. 3, no. 1, pp. 121–129, 1988.

[14] F. V. Lopes, K. M. Silva, F. B. Costa, W. L. A. Neves, and D. Fernandes, "Real-time traveling-wave-based fault location using two-terminal unsynchronized data," *IEEE Transactions on Power Delivery*, vol. 30, no. 3, pp. 1067–1076, 2015.

[15] M. Kezunovic and B. Perunicic, "Automated transmission line fault analysis using synchronized sampling at two ends," *IEEE Transactions on Power Systems*, vol. 11, no. 1, pp. 441–447, 1996.

[16] A. L. Dalcastagnê, S. Noceti Filho, H. H. Zurn, and R. Seara, "An iterative two-terminal fault-location method based on unsynchronized phasors," *IEEE Transactions on power delivery*, vol. 23, no. 4, pp. 2318–2329, 2008.

[17] Y. Liao and N. Kang, "Fault-location algorithms without utilizing line parameters based on the distributed parameter line model," *IEEE Transactions on Power Delivery*, vol. 24, no. 2, pp. 579–584, 2009.

[18] S. L. Zimath, M. A. Ramos, J. S. Filho, J. M. Beck, and N. Mueller, "Traveling wave-based fault location experiences," in *2010 63rd Annual Conference for Protective Relay Engineers*, pp. 1–7, 2010.

[19] S. L. Nilsson, M. Lima, and D. J. Young, "Ac system characteristics," *Flexible AC Transmission Systems: FACTS*, pp. 15–50, 2020.

[20] P. Jafarian and M. Sanaye-Pasand, "A traveling-wave-based protection technique using wavelet/pca analysis," *IEEE Transactions on Power Delivery*, vol. 25, no. 2, pp. 588–599, 2010.

[21] L. V. Bewley, *Traveling waves on transmission systems*. Wiley New York, 1951.

[22] R. J. Hamidi and H. Livani, "Traveling-wave-based fault-location algorithm for hy-

brid multiterminal circuits," *IEEE Transactions on Power Delivery*, vol. 32, no. 1, pp. 135–144, 2017.

[23] H. W. Johnson and M. Graham, *High-speed signal propagation: advanced black magic*. Prentice Hall Professional, 2003.

[24] K. A. Saleh, A. Hooshyar, and E. F. El-Saadany, "Ultra-high-speed traveling-wave-based protection scheme for medium-voltage dc microgrids," *IEEE Transactions on Smart Grid*, vol. 10, no. 2, pp. 1440–1451, 2019.

[25] H. Jia *et al.*, "An improved traveling-wave-based fault location method with compensating the dispersion effect of traveling wave in wavelet domain," *Mathematical Problems in Engineering*, vol. 2017, 2017.

[26] E. O. Schweitzer, A. Guzmán, M. V. Mynam, V. Skendzic, B. Kasztenny, and S. Marx, "Locating faults by the traveling waves they launch," in *2014 67th Annual Conference for Protective Relay Engineers*, pp. 95–110, 2014.

[27] J. A. Hogan and J. D. Lakey, *Time-frequency and time-scale methods: adaptive decompositions, uncertainty principles, and sampling*. Springer, 2005.

[28] Y. Meyer, *Wavelets and Operators: Volume 1*. No. 37, Cambridge university press, 1992.

[29] T. B. Littler and D. J. Morrow, "Wavelets for the analysis and compression of power system disturbances," *IEEE Transactions on Power Delivery*, vol. 14, no. 2, pp. 358–364, 1999.

[30] A. Osman and O. Malik, "Transmission line distance protection based on wavelet transform," *IEEE Transactions on Power Delivery*, vol. 19, no. 2, pp. 515–523, 2004.

[31] A. Osadchiy, A. Kamenev, V. Saharov, and S. Chernyi, "Signal processing algorithm based on discrete wavelet transform," *Designs*, vol. 5, no. 3, p. 41, 2021.

[32] V. Gonzalez-Sanchez, V. Torres-García, and D. Guillen, "Fault location on transmission lines based on travelling waves using correlation and modwt," *Electric Power Systems Research*, vol. 197, p. 107308, 2021.

[33] M. Korkali, H. Lev-Ari, and A. Abur, "Traveling-wave-based fault-location technique for transmission grids via wide-area synchronized voltage measurements," *IEEE Transactions on Power Systems*, vol. 27, no. 2, pp. 1003–1011, 2012.

[34] P. E. Argyropoulos and H. Lev-Ari, "Wavelet customization for improved fault-

location quality in power networks," *IEEE Transactions on Power Delivery*, vol. 30, no. 5, pp. 2215–2223, 2015.

[35] F. Lopes, B. Küsel, and K. Silva, "Traveling wave-based fault location on half-wavelength transmission lines," *IEEE Latin America Transactions*, vol. 14, no. 1, pp. 248–253, 2016.

[36] M. da Silva, D. V. Coury, M. Oleskovicz, and C. Segatto, "Combined solution for fault location in three-terminal lines based on wavelet transforms," *IET Generation, Transmission Distribution*, vol. 4, no. 1, pp. 94–103, 2010.

[37] E. Ngu and K. Ramar, "A combined impedance and traveling wave based fault location method for multi-terminal transmission lines," *International Journal of Electrical Power Energy Systems*, vol. 33, no. 10, pp. 1767–1775, 2011.

[38] T. Nagasawa, M. Abe, N. Otsuzuki, T. Emura, Y. Jikihara, and M. Takeuchi, "Development of a new fault location algorithm for multi-terminal two parallel transmission lines," *IEEE Transactions on Power Delivery*, vol. 7, no. 3, pp. 1516–1532, 1992.

[39] M. Parsi, P. Crossley, P. Luigi Dragotti, and D. Cole, "Wavelet based fault location on power transmission lines using real-world travelling wave data," *Electric Power Systems Research*, vol. 186, p. 106261, 2020.

[40] M. Parsi and P. A. Crossley, "Optimised time for travelling wave fault locators in the presence of different disturbances based on real-world fault data," *IEEE Open Access Journal of Power and Energy*, vol. 8, pp. 138–146, 2021.

[41] A. Ukil and R. ivanovi, "Application of abrupt change detection in power systems disturbance analysis and relay performance monitoring," *IEEE Transactions on Power Delivery*, vol. 22, no. 1, pp. 59–66, 2007.

[42] E. Clarke, *Circuit analysis of AC power systems: symmetrical and related components*, vol. 1. Wiley, 1943.

[43] D. O. Aikhuele and F. M. Turan, "An exponential-related function for decision-making in engineering and management," *Open Engineering*, vol. 7, no. 1, pp. 153–160, 2017.

[44] A. Grinsted, J. C. Moore, and S. Jevrejeva, "Application of the cross wavelet transform and wavelet coherence to geophysical time series," *Nonlinear processes in geophysics*, vol. 11, no. 5/6, pp. 561–566, 2004.

BIOGRAPHICAL SKETCH

Background: Born and raised in Tabriz/Iran

Education:

Bachelor of Science in Electrical Engineering, Iran University of Science and Technology, Tehran

Master of Science in Electrical Engineering, Shahid Beheshti University, Tehran

Research Focus: Power System Analysis, Energy Management Systems, Protection of Power Systems and Fault Location

Doctoral Studies: Pursuing a Doctor of Philosophy (Ph.D.) in Electrical Engineering, Syracuse University

Extensive research in Fault location in Power Systems using Traveling Waves, Application of Wavelets in Processing High-Frequency Measurements in Power Systems